

Chapter 14

Atomistic Pseudopotential Theory of Droplet Epitaxial GaAs/AlGaAs Quantum Dots

Jun-Wei Luo, Gabriel Bester, and Alex Zunger

Abstract In this chapter, following the introduction to the basic electronic properties of semiconductor quantum dots (QDs), we first briefly introduce our atomistic methodology for multi-million atom nanostructures, which is based on the empirical pseudopotential method for the solution of the single-particle problem combined with the configuration interaction (CI) scheme for the many-body problem which were developed in the solid-state theory group at the National Renewable Energy Laboratory over the past two decades. This methodology, described in Sect. 14.2, can be used to provide quantitative predictions of the electronic and optical properties of colloidal nanostructures containing thousands of atoms as well as epitaxial nanostructures containing several millions of atoms. In Sect. 14.3, we show how the multi-exciton spectra of a droplet epitaxy QD encodes nontrivial structural information that can be uncovered by atomistic many-body pseudopotential calculations. In Sect. 14.4, we investigate the vertical electric field tuning of the fine-structure splitting (FSS) in several InGaAs and GaAs QDs using our atomistic methodology. We reveal the influence of the atomic-scale structure on the exciton FSS in QDs. Finally, a comprehensive and quantitative analysis of the different mechanisms leading to HH–LH mixing in QDs is presented in Sect. 14.5. The novel quantum transmissibility of HH–LH mixing mediated by intermediate states is discovered. The design rules for optimization of the HH–LH mixing in QDs are given in this section.

J.-W. Luo (✉)

National Renewable Energy Laboratory, Golden, CO 80401, USA

e-mail: jun-wei.luo@nrel.gov

G. Bester

Max-Planck-Institut für Festkörperforschung, Heisenbergstrasse 1, 70569 Stuttgart, Germany

e-mail: G.Bester@fkf.mpg.de

A. Zunger

University of Colorado, Boulder, CO 80309, USA

e-mail: alex.Zunger@colorado.edu

14.1 Introduction

Until recently, epitaxial quantum dots (QDs) were mostly made by a growth protocol (“Stranski–Krastanov”, or SK) [1–3] requiring that the QD material has a significantly different lattice constant (generally larger) than the substrate on which it is grown, e.g., InAs-on-GaAs [1] or InP-on-GaP [3]. Lattice-matched material pairs such as GaAs on AlGaAs or InAs on GaSb were excluded until recently. The advent of the “droplet epitaxy” growth mode [4–6] (involving the growth of cation-element droplets on a substrate and subsequently their crystallization into QDs by incorporation of the anion element) has enabled the epitaxial growth of lattice-matched pairs, thus opening a window to the understanding of the physics of confinement in unstrained semiconductor material such as GaAs. GaAs QDs have recently also been grown using an alternative approach [7–11] where nanoholes are etched on the surface of an AlGaAs layer. The holes are etched by arsenic debt epitaxy (also referred to as local droplet etching) and filled with GaAs. Migration of the GaAs toward the bottom of the holes leads to GaAs QD formation. The QDs are subsequently capped with AlGaAs. The lattice-mismatch-induced strain in In(Ga)As/GaAs QDs represents a main difference from unstrained GaAs/AlGaAs QDs and it markedly modifies the bulk band structure. Figure 14.3 shows that the built-in biaxial strain present in InAs QDs embedded in GaAs [12, 13] lifts the degeneracy of the bulk heavy-hole (HH) and light-hole (LH) bands by as much as 0.18 eV, without considering the quantum confinement effect. The built-in shear strain also couples the HH and LH bands and it appears in the Pikus–Bir Hamiltonian as off-diagonal term [12, 13]. Furthermore, in the droplet case, GaAs represents the QD material, whereas in InAs/GaAs the barrier is GaAs and the QD is InAs. Therefore, the conduction and valence band offsets (confinement potentials) in these two types of QDs are different as shown in Fig. 14.3. Moreover, InAs and GaAs differ in bandgap, electron, and hole effective masses and the relative positions of the conduction band states at Γ , X , and L . It is thus by no means obvious that there will be a similarity in the electronic structure results of GaAs/AlGaAs with InAs/GaAs. Indeed, we find a very different electronic structure in one critical aspect: the order of hole states. In GaAs/AlGaAs the LH-derived S-like state lies between two HH-derived P-like hole states, whereas in InAs/GaAs the LH state is well below the HH-derived P-like hole states.

The symmetry reduction of low-dimensional nanostructures can lead to mixing between electronic states not only from the same bulk band [14] but also from different valleys of the Brillouin zone and different bulk bands [15–18], which are forbidden in their parent bulk semiconductors. Among various possibilities of electronic state mixing, the HH–LH mixing in semiconductor QDs has attracted much attention over the last few years for its profound effects on electronic and optical properties. Specifically, HH–LH mixing is essential to tune the exciton fine-structure splitting (FSS) of an epitaxial grown QD using a vertical electric field [19–21], since it can manipulate FSS only via acting on the bulk $|Z\rangle$ component of the Bloch functions. The QD ground hole state has dominantly bulk HH

character [21], whereas the bulk HH band, $|3/2, \pm 3/2\rangle = \mp(|X\rangle \pm i|Y\rangle)|\uparrow, \downarrow\rangle/\sqrt{2}$, contains exclusively $|X\rangle, |Y\rangle$ components, and the bulk LH band $|3/2, \pm 1/2\rangle = (1/\sqrt{3})[(|X\rangle \pm i|Y\rangle)|\downarrow, \uparrow\rangle + \sqrt{2}|Z\rangle|\uparrow, \downarrow\rangle]$ contains $|Z\rangle$ component. Thus, mixing LH with HH leads to the control of the FSS via vertical electric field F_z . HH–LH mixing also leads to fast spin decoherence of HH-dominated QD holes [22] by introducing additional efficient spin relaxation channels belong to LH band. In addition, both experimentally and theoretically observed optical polarization anisotropy of neutral excitons (e.g., X^0 and XX^0) and charged trion (e.g., X^{-1} and X^{+1}) radiative recombination is known to arise from HH–LH mixing [23–27].

In the remainder of this chapter, we first briefly introduce our atomistic methodology for multi-million atom nanostructures, which is based on the empirical pseudopotential method [28], combined with the configuration interaction (CI) scheme for the many-body problem developed by solid-state theory group at NREL over the past two decades. This methodology, described in Sect. 14.2, can be used to provide quantitative predictions of the electronic and optical properties of colloidal nanostructures [15, 29–34] containing thousands of atoms as well as epitaxial nanostructures [17, 18, 21, 35–41] containing several millions of atoms. In Sect. 14.3, we then show how the multi-exciton spectra of an unstrained GaAs QD encodes nontrivial structural information that can be uncovered by atomistic many-body pseudopotential calculations. In Sect. 14.4, we investigate the vertical electric field tuning of the FSS in several InGaAs and GaAs QDs and reveal the influence of the atomic-scale structure on the exciton FSS in QDs. Finally, in Sect. 14.5 a comprehensive and quantitative analysis of the different mechanisms leading to HH–LH mixing in QDs is presented. We specifically highlight the discovery of the quantum transmissibility of the HH–LH mixing mediated by QD intermediate states. The design rules for optimization of the HH–LH mixing in QDs are given in this section.

14.2 Atomistic Many-Body Pseudopotential Method for Multi-million Atom Nanostructures

The basis of our methodology, which was reviewed recently by one of us in [42], is divided into four parts, atomic position relaxation, Schrödinger equation for single-particle electronic states, many-body Hamiltonian accounting for Coulomb interaction and correlation effect, and post-processors for optical properties, all feeding into each other. The calculation of the single-particle electronic states requires the input of the geometry and relaxation of the atomic positions to minimize strain. The development of empirical pseudopotentials for each atom type is the prerequisite for the Schrödinger equation. The ensuing eigenfunctions are fed into a configuration interaction (CI) treatment

wavefunctions, observables can be obtained through the use of post-processor tools. These different components will be briefly discussed below and we refer to [28, 42–47] for more detail.

Calculation of Atomistic Strain and Atom Position Relaxation. The first step is to construct a simulation cell (supercell) containing a QD with an assumed shape, size, and composition (gradient) and place the atoms on ideal zinc-blende crystal sites. The atoms within the supercell are then allowed to relax in order to minimize the strain energy using Keating's valence force field (VFF) method [45, 46, 48], including bond stretching, bond bending, and bond bending–bond stretching interactions:

$$\begin{aligned}
 E_{\text{VFF}} = & \sum_i \sum_j^{m_i} \frac{3}{8} \left[\alpha_{ij}^{(1)} \Delta d_{ij}^2 + \alpha_{ij}^{(2)} \Delta d_{ij}^3 \right] \\
 & + \sum_i \sum_{k < j}^{m_i} \frac{3\beta_{jik}}{8d_{ij}^0 d_{ik}^0} \left[(\mathbf{R}_j - \mathbf{R}_i) \cdot (\mathbf{R}_k - \mathbf{R}_i) - \cos \theta_{jik}^0 d_{ij}^0 d_{ik}^0 \right] \\
 & + \sum_i \sum_{k < j}^{m_i} \frac{3\sigma_{jik}}{8\sqrt{d_{ij}^0 d_{ik}^0}} \Delta d_{ij} \left[(\mathbf{R}_j - \mathbf{R}_i) \cdot (\mathbf{R}_k - \mathbf{R}_i) - \cos \theta_{jik}^0 d_{ij}^0 d_{ik}^0 \right], \quad (14.1)
 \end{aligned}$$

where $\Delta d_{ij} = \left[(\mathbf{R}_i - \mathbf{R}_j)^2 - (d_{ij}^0)^2 \right] / d_{ij}^0$, \mathbf{R}_i is the coordinate of atom i , d_{ij}^0 is the ideal (unrelaxed) bond length between atoms i and j , and θ_{ijk}^0 is the ideal (unrelaxed) angle of bonds $j-i-k$. $\sum_i^{m_i}$ denotes summation over the nearest neighbors of atom i ($m_i = 4$ for diamond, zinc-blende, and wurtzite crystal structures). The bond stretching, bond-angle bending, and bond-length–bond-angle interaction coefficients $\alpha_{ij}^{(1)}$ ($\equiv \alpha$), β_{jik} , and σ_{jik} are directly related to the elastic constants in bulk materials [46]:

$$\begin{aligned}
 C_{11} + 2C_{12} &= \sqrt{\frac{3}{4d^0}} (3\alpha + \beta - 6\sigma) \\
 C_{11} - C_{12} &= \sqrt{\frac{3}{d^0}} \beta \\
 C_{44} &= \sqrt{\frac{3}{d^0}} \frac{\alpha\beta - \sigma^2}{\alpha + \beta + 2\sigma}. \quad (14.2)
 \end{aligned}$$

The second-order bond-stretching term is included to correct the pressure dependence of Young's modulus dB/dP , where $B = (C_{11} + 2C_{12})/3$. After the atomic positions are relaxed by minimizing E_{VFF} , the local strain tensor ε at a cation site is calculated by considering a tetrahedron formed by four nearest neighboring anions [45]. The distorted (relaxed) tetrahedron edges (\mathbf{R}_{12} , \mathbf{R}_{23} , \mathbf{R}_{34}) are related to the ideal (unrelaxed) tetrahedron edges (\mathbf{R}_{12}^0 , \mathbf{R}_{23}^0 , \mathbf{R}_{34}^0) via the local strain tensor ε as illustrated in Fig. 14.1:

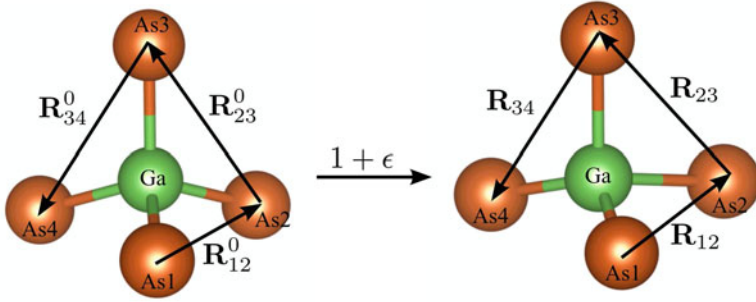


Fig. 14.1 Schematic to illustrate how the local strain is calculated in zinc blende semiconductors. For a cation Ga (or In), three vectors (\mathbf{R}_{12} , \mathbf{R}_{23} , \mathbf{R}_{34}) forming a distorted tetrahedron after atomic relaxation are related to the equivalent vectors (\mathbf{R}_{12}^0 , \mathbf{R}_{23}^0 , \mathbf{R}_{34}^0) of an ideal tetrahedron via the strain tensor ϵ

$$(\mathbf{R}_{12}, \mathbf{R}_{23}, \mathbf{R}_{34}) = (1 + \epsilon) \cdot (\mathbf{R}_{12}^0, \mathbf{R}_{23}^0, \mathbf{R}_{34}^0). \quad (14.3)$$

Solving the Schrödinger Equation for the Nanostructure. The single-particle QD electronic states are obtained from solving the empirical pseudopotential Schrödinger equation [35, 46, 47],

$$\left(-\frac{\hbar^2}{2m} \nabla^2 + V(\mathbf{r}) + |e|\mathbf{F} \cdot \mathbf{r} \right) \psi_i(\mathbf{r}, \sigma) = \epsilon_i \psi_i(\mathbf{r}, \sigma), \quad (14.4)$$

within a basis of linear combination of strained Bloch bands (SLCBB) [43]. Here $\{\epsilon_i, \psi_i(\mathbf{r}, \sigma)\}$ are the eigenvalues and eigenstates of state i with spin σ . The bare electron mass is given by m and \hbar is Planck's constant. An external electric field \mathbf{F} is optionally applied in the supercell [49] for investigating the influence of electric field on QD electronic structure and excitons. The crystal (dot + matrix) potential $V(\mathbf{r})$ is a superposition of overlapping screened atomic (pseudo) potentials centered at the atomic positions:

$$V(\mathbf{r}) = \sum_n \sum_{\alpha} \hat{v}_{\alpha}(\mathbf{r} - \mathbf{R}_n - \mathbf{d}_{\alpha}), \quad (14.5)$$

where $\hat{v}_{\alpha}(\mathbf{r} - \mathbf{R}_n - \mathbf{d}_{\alpha})$ pertains to atom-type α at site \mathbf{d}_{α} in the n th primary cell \mathbf{R}_n [46, 47]. Thus, it forces upon eigenstates the correct atomically resolved symmetry. The atomic potentials \hat{v}_{α} were empirically fit to experimental transition energies, spin-orbit splittings, effective masses, deformation potentials of the bulk materials, as well as the band offsets between two materials in a heterostructure [46, 47]. Readers wishing to review the fitting of the GaAs/AlAs and InAs/GaAs pseudopotentials in detail are referred to [47] and [46], respectively. Figure 14.2 shows the calculated square of the single-particle wave functions of the four lowest electron states and the four highest hole states for both strain-free GaAs/AlGaAs and

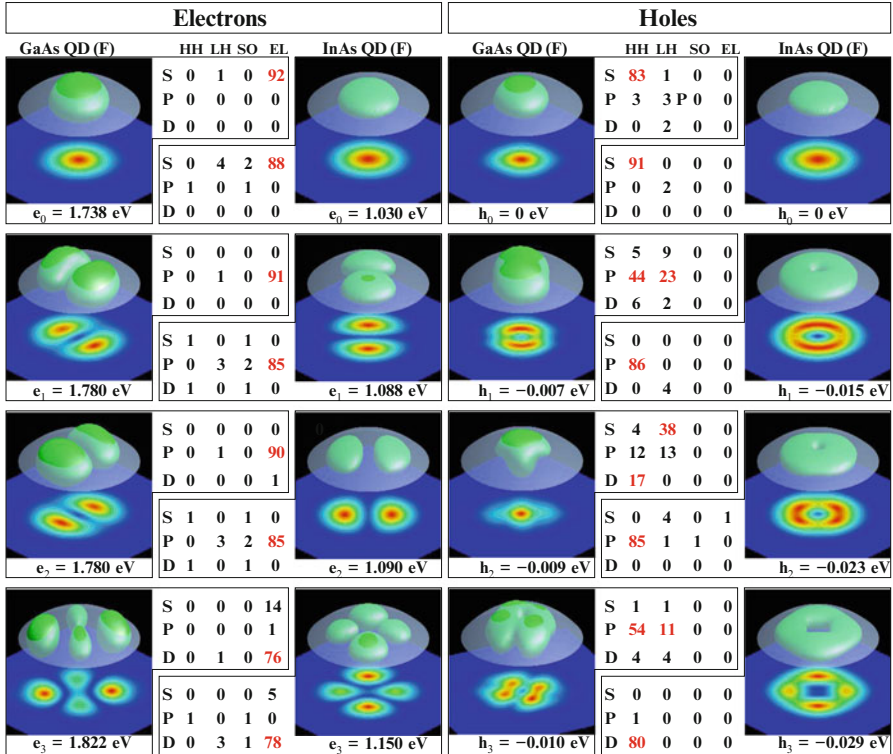


Fig. 14.2 The squared wave functions (3D isosurface and 2D in-plane mapping) of the first four electron and first four hole states for an unstrained GaAs/Al_{0.3}Ga_{0.7}As QD and a strained InAs/GaAs QD, with the same lens shape and the same size (25.2 nm base and 3 nm height). For analysis purposes, we project the wave functions of the QDs on bulk heavy-hole (HH), light-hole (LH), split-off (SO) bands, and the lowest conduction band (CB). The wave functions are further decomposed with respect to their axial angular momentum components (S, P, D)

strained InAs/GaAs QDs with a lens shape. The orbital characters of each state are obtained by decomposing our atomistic electron and hole states with respect to their axial angular momentum components (S, P, D, ...). The bulk Bloch band character of the QD electronic states are gained by projecting them onto bulk Bloch bands at the Γ -point, including HH ($|3/2, \pm 3/2\rangle$), LH ($|3/2, \pm 1/2\rangle$), spin-orbit split (SO) ($|1/2, \pm 1/2\rangle$), bands as well as conduction bands (CB).

Solution of the Many-Body Problem. Once the single particle states of the QD are obtained, the excitonic energies and wave functions, including many-body interactions are calculated in the framework of the CI scheme [44]. In this approach, the excitonic wave functions $\Psi^{(i)}$ are expanded in terms of single-substitution Slater determinants $\Phi_{\nu,c}$, constructed by promoting an electron from the occupied single-particle state ν to the unoccupied single-particle state c :

$$\Psi^{(i)} = \sum_{v=1}^{N_v} \sum_{c=1}^{N_c} C_{v,c}^{(i)} \Phi_{v,c}. \quad (14.6)$$

The coefficients $C_{v,c}^{(i)}$ of the CI expansion are calculated by diagonalizing the CI Hamiltonian for a single exciton:

$$H_{vc,v'c'} \equiv \langle \Psi_{v,c} | H_{CI} | \Psi_{v',c'} \rangle = (\varepsilon_c - \varepsilon_v) \delta_{v,v'} \delta_{c,c'} - J_{vc,v'c'} + K_{vc,v'c'}, \quad (14.7)$$

where the Coulomb and exchange integrals $J_{vc,v'c'}$ and $K_{vc,v'c'}$ are, respectively, given by

$$J_{vc,v'c'} = e^2 \sum_{\sigma,\sigma'} \int \int \frac{\Psi_v^*(\mathbf{r}, \sigma) \Psi_c^*(\mathbf{r}', \sigma') \Psi_{v'}(\mathbf{r}, \sigma) \Psi_{c'}(\mathbf{r}', \sigma')}{\bar{\varepsilon}(\mathbf{r}, \mathbf{r}') |\mathbf{r} - \mathbf{r}'|} d\mathbf{r} d\mathbf{r}' \quad (14.8)$$

$$K_{vc,v'c'} = e^2 \sum_{\sigma,\sigma'} \int \int \frac{\Psi_v^*(\mathbf{r}, \sigma) \Psi_c^*(\mathbf{r}', \sigma') \Psi_{c'}(\mathbf{r}, \sigma) \Psi_{v'}(\mathbf{r}', \sigma')}{\bar{\varepsilon}(\mathbf{r}, \mathbf{r}') |\mathbf{r} - \mathbf{r}'|} d\mathbf{r} d\mathbf{r}'. \quad (14.9)$$

The Coulomb potential in the two equations above are screened using a position-dependent and size-dependent screening function $\bar{\varepsilon}(\mathbf{r}, \mathbf{r}')$ [44]. The excitonic wavefunctions of Eq. (14.6) are built using 6 valence and 6 conduction band states, including envelope functions with S, P, and D orbital character.

Post-processor Tools. The modification of the potential due to strain can be obtained from the Pikus–Bir Hamiltonian [12] once the atoms within the supercell are relaxed using the VFF method [45, 46, 48] and the strain tensor has been calculated. A comprehensive study of the effect of strain on the band structure has been performed by Bir and Pikus [13]. Here, a simplified Pikus–Bir Hamiltonian is used to describe the strain-modified confinement potentials, which is, however, not used in our atomistic pseudopotential calculation of the single-particle eigenstates, but serves only as illustration of strain effects. Following [12], in which the model is written in real space, the strain-modified conduction band state is given by

$$E_c(\mathbf{r}) = E_c^0(\mathbf{r}) + a_c(\mathbf{r}) Tr[\varepsilon(\mathbf{r})], \quad (14.10)$$

where $E_c^0(\mathbf{r})$ is the conduction band minimum (CBM) of bulk material at \mathbf{r} and a_c is the hydrostatic deformation potential of the CBM, generally at Γ . For valence bands including spin–orbit coupling, the Pikus–Bir Hamiltonian is

$$H_v(\mathbf{r}) = H^{SO} + a_v Tr[\varepsilon(\mathbf{r})] \quad (14.11)$$

$$-b_v \left[\begin{pmatrix} -2 & 0 & 0 \\ 0 & 1 & 0 \\ 0 & 0 & 1 \end{pmatrix} \varepsilon_{xx} + \begin{pmatrix} 1 & 0 & 0 \\ 0 & -2 & 0 \\ 0 & 0 & 1 \end{pmatrix} \varepsilon_{yy} + \begin{pmatrix} 1 & 0 & 0 \\ 0 & 1 & 0 \\ 0 & 0 & -2 \end{pmatrix} \varepsilon_{zz} \right]$$

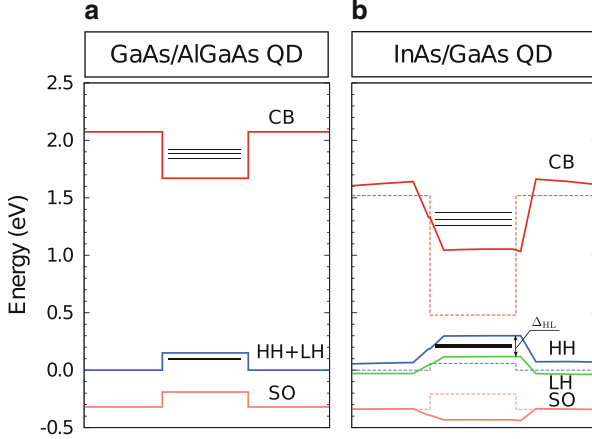


Fig. 14.3 Confinement potential of the lowest conduction band (CB), heavy-hole (HH), light-hole (LH), and split-off (SO) bands for (a) a strain-free GaAs/Al_{0.3}Ga_{0.7}As QD and (b) a strained InAs/GaAs QD with lens shape of base size 30 and 3 nm height. The *dashed lines* in (b) represent the bulk energy levels without considering strain. Δ_{HL} is built-in strain-induced splitting of bulk HH and LH bands

$$-\sqrt{3}d_v \left[\begin{pmatrix} 0 & -1 & 0 \\ -1 & 0 & 0 \\ 0 & 0 & 0 \end{pmatrix} \varepsilon_{xy} + \begin{pmatrix} 0 & 0 & 0 \\ 0 & 0 & -1 \\ 0 & -1 & 0 \end{pmatrix} \varepsilon_{yz} + \begin{pmatrix} 0 & 0 & -1 \\ 0 & 0 & 0 \\ -1 & 0 & 0 \end{pmatrix} \varepsilon_{zx} \right],$$

where H^{SO} is the spin-orbit Hamiltonian [12], a_v is the hydrostatic deformation potential of the VBM, b_v is the biaxial deformation of the valence band maximum (VBM), and d_v is the deformation potential due to shear strain. The value of deformation potentials a_c , a_v , b_v , and d_v are taken from [12, 50]. The calculated strain-modified confinement potentials of a strained InAs/GaAs and an unstrained GaAs/AlGaAs QD using the Pikus-Bir model, as well as the natural band offsets at their equilibrium lattice constants are shown in Fig. 14.3.

After we have calculated the many-body wavefunctions, we have access to observables through the use of post-processor tools. For example, the excitonic optical-absorption spectrum $I(E)$ are calculated with the CI eigenstates of Eq. (14.6) by using Fermi's golden rule [51]:

$$I(E) = \sum_v |M_v|^2 \exp \left[- \left(\frac{E - E_v}{\sigma} \right)^2 \right], \quad (14.12)$$

where $M_v = \sum_{h_i, e_j} C^{(v)}(h_i, e_j) \langle \psi_{h_i} | \hat{p} | \psi_{e_j} \rangle$ is the transition dipole matrix between hole state h_i and electron state e_j , E_v is the exciton energy and the broadening of spectral lines modeled by a chosen σ .

14.3 Geometry of Epitaxial GaAs/(Al,Ga)As QDs as Seen by Excitonic Spectroscopy

Molecular spectroscopy has always been intimately connected with molecular structure and symmetry through fundamental interpretative constructs such as symmetry-mandated selection rules, level degeneracies, and polarization [52]. Yet, the spectroscopy of epitaxial semiconductor QDs—large simple molecules made of 10^3 – 10^6 atoms such as Si, InAs, or GaAs—has been largely conducted and interpreted without basic knowledge of the underlying structure. Indeed, the extremely rich (10–20 lines), high-resolution (~ 10 μ eV) single-dot excitonic spectra of such simple “macromolecules” being now measured almost routinely [1, 2, 53–56] has not been accompanied by detailed structural information, other than cross-sectional scanning tunneling microscopy (XSTM) measurements [57, 58] which, however, can produce a range of diverging structures from the same measured relaxation profile on the same QD [39]. A possibly more accurate structure profile of epitaxy QDs can be indirectly obtained from a full three-dimensional electron density map measured by 9 coherent Bragg rod analysis (COBRA) method [59]. Attempts to bridge the gap between spectra and structure have recently been made in the context of self-assembled (strained) In(Ga)As/GaAs QDs by combining measured excitonic spectra with XSTM structural assessment of the same QD sample, using a quantitative excitonic theory as the bridge. It was found [39] that the calculated excitonic spectra produced by using as input a range of structural models offered by XSTM conflicted with the experimental spectra in a number of crucial aspects. However, a structure derived theoretically by matching the calculated spectra with experiment did agree with the basic data used to derive XSTM structural models (i.e., the measured outer relaxation profile of the cleaved QD). It was concluded that high-resolution excitonic spectra contain significant structural information that can be unearthed using theory as a mining tool.

Recent XSTM measurements [57] suggest that droplet GaAs QDs have Gaussian shape instead of the lens shape often deduced from atomic force microscope (AFM) measurements [56, 60–62] and QD heights of around 14 nm [57, 62]. The exciton band gap measured by optical spectroscopy is about 1.7–1.9 eV [25, 56, 60, 63, 64]. In [41] we discussed the spectra vs. structure link for such QDs. We found that the GaAs QDs grown by droplet epitaxy have indeed a Gaussian-shape, as suggested by the XSTM measurements [57]. However, we found that QDs as seen by optical spectroscopy correspond to QDs with 2–4 nm height rather than the 14 nm determined by XSTM. The fact that XSTM sees tall QDs and spectroscopy sees flat QDs points to the fact that different QDs must have been probed. This was uncovered by theoretical simulations showing that the two experiments could not possibly correspond to the same QD.

Measured Structure. GaAs/GaAlAs QDs grown by droplet epitaxy in Sakoda’s group [63] were initially described, on the basis of AFM measurements of uncapped QDs [62], as being lens shaped [56, 60–62] (schematic in left inset of Fig. 14.4),

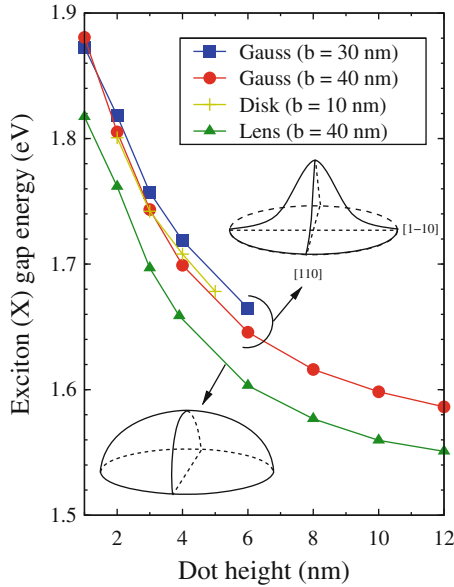


Fig. 14.4 Atomistic many-body pseudopotential calculated exciton emission energy of Gaussian-shaped, lens-shaped, and disk-shaped GaAs/Al_{0.3}Ga_{0.7}As QDs (base size in diameter given in *parentheses*) as a function of QD height. The base diameter of Gaussian-shaped QD is defined by the largest QD lateral size, which is truncated by the requirement that the QD material must be thicker than 1 ML. Taken from [41]. ©(2011) by the American Physical Society

with averaged $[1\bar{1}0]$ -elongated base size of 70×50 nm (spread $\pm 10\%$) and a QD height of 14 nm (spread $\pm 19\%$) [62]. Subsequently, XSTM measurement of these capped QDs were performed by Keizer et al. [57] showing instead a rather different, Gaussian shape (schematic in right inset to Fig. 14.4) with an average base size of 40 nm, height of 14 nm, and a size distribution of 10–20%.

Spectra of Single Exciton. The measured spectroscopy [25, 56, 60, 63, 64] of the QDs grown by Sakoda's group [63] shows that the fundamental exciton emission from many different spectroscopy measurements were in a range of 1.7–1.9 eV.

Calculated Spectra for the Measured Structure Lead to Conflicts with the Assumed Structure. We have calculated the exciton gap energy of lens-shaped, Gaussian-shaped, and disk-shaped strain-free GaAs/AlGaAs QDs using our atomistic many-body pseudopotential method (Fig. 14.4). Notwithstanding the shape, the QDs with calculated exciton energy in the range of the experimental measured exciton energy of 1.7–1.9 eV have a much smaller QD height, of only 1–4 nm compared to the experimentally stated value (~ 14 nm) by both AFM [62] and XSTM [57] approaches. This discrepancy, being well outside the measured size distribution in the sample, indicates that the QDs measured by AFM or XSTM are not the same

as the QDs seen by optical spectroscopy. We conclude¹ that the QD, the height of which was measured to be 14 nm in [57, 62], is not the same QD that was used in [25, 56, 60, 63, 64] to measure the band gap and exciton fine structure. It is worth mentioning that the QD height decreases from 14 nm when the QDs are grown by droplet epitaxy on a (001)-oriented GaAs substrate [57] to much smaller value of 2.3 ± 0.6 nm when they are grown on a (311)A-oriented GaAs substrate [65]. However, the XSTM [57] and spectroscopy [25, 56, 56, 60, 63] measurements considered here, as well as theory, are all on (001) substrates.

Whereas to first order, the magnitude of the excitonic emission energy reveals information mostly on the QD height, a more detailed measurement can also distinguish different QD shapes. We see from Fig. 14.4 that for the same base size and QD height, the lens-shape QDs have an exciton gap energy that is smaller by as much as ~ 40 meV than that of Gaussian-shaped QDs and that this is so in a wide range of QD heights of 1–12 nm. If droplet epitaxy grown GaAs/AlGaAs QDs are known to be either lens shaped or Gaussian shaped, this exciton shift is large enough to distinguish the QD shape if the base size, QD height, and exciton energy are accurately measured.

The Shape of the QD as Seen by the Sequence of Multi-exciton Lines. Experimentally, different types of excitons can be created: neutral monoexciton X^0 (1e,1h) or neutral biexciton XX^0 (2e,2h), as well as charged excitons such as positive trion X^+ (1e,2h), negative trion X^- (2e,1h), positive biexciton XX^+ (2e,3h), and negative biexciton XX^- (3e,2h), etc. Figure 14.5 shows the calculated emission spectrum when a single electron–hole pair recombines within such a multi-exciton complex [66]. The spectra consist of a few lines. Specially for XX^+ and XX^- we see several manifolds of four and two lines, respectively, due to various S and P recombination channels and e–h exchange interaction induced FSS of multi-exciton complexes. The emission energy reflects both direct Coulomb interactions and correlation effects between holes and electrons; these interactions ultimately reflect the overlap of the corresponding wave functions which is sensitive to the shape and size of the QD. Such complex and implicit dependences between the sequence of multi-exciton lines (“multi-exciton barcode”) and QD structure were used recently to decipher structural features from excitonic features. It was proposed [39] that such barcodes consisting of X , X^+ , X^- , XX , XX^+ , XX^- , and X^{-2} lines can be correlated with geometrical features of the strained SK-grown InAs/GaAs QDs.

Here we will use this barcoding approach to unearth structural features of another class of QDs based on unstrained, droplet epitaxy grown GaAs/GaAlAs. For this purpose we have calculated the sequence of multi-excitonic lines for a large number of QDs with three different basic shapes (lens shape, Gaussian shape, and disk shape) and many structural parameters within these shapes (height, base size, and shape anisotropy). Using this barcoding method, we can build a link between the structure of strain-free GaAs/AlGaAs QDs and their excitonic emission spectra.

¹We are grateful to Prof. P.M. Koenraad and Dr. M. Takaaki for clarifying to us now that the QDs used in XSTM were different than those used for PL measurements.

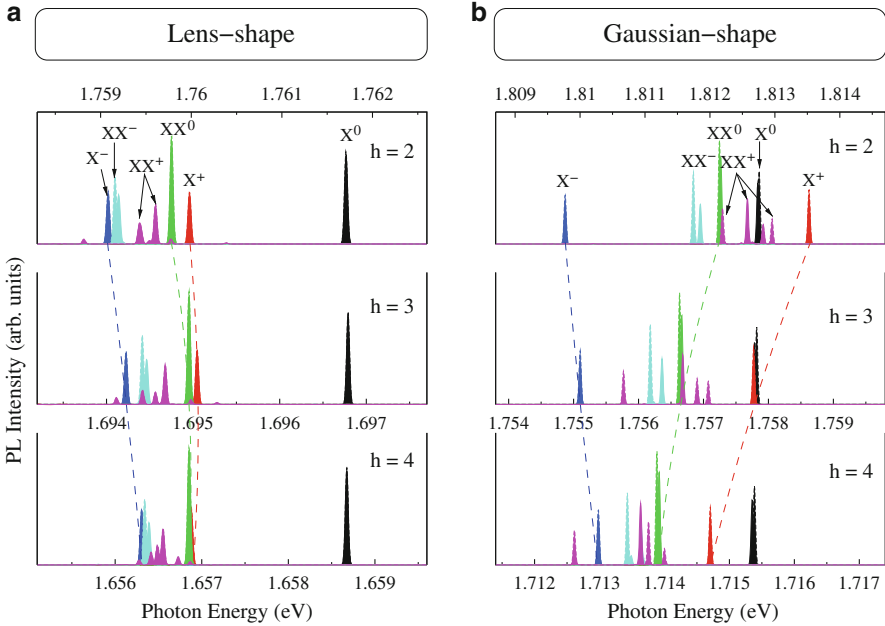


Fig. 14.5 Excitonic emission spectrum of (a) symmetric lens-shaped and (b) symmetric Gaussian-shaped GaAs/Al_{0.3}Ga_{0.7}As QDs with base size of $b = 40 \times 40$ nm and QD height $h = 2, 3,$ and 4 nm. Taken from [41]. ©(2011) by the American Physical Society

However, at present, the available experimentally measured excitonic emission spectrum of such QDs includes only neutral monoexciton X^0 , positive and negative trions X^+ and X^- , and neutral biexciton XX^0 transitions [25, 56, 56, 60, 63]. Figure 14.5 shows the atomistic calculated emission spectra (where we have aligned the energy of the monoexciton X^0 lines) for lens-shaped (Fig. 14.5a) and Gaussian-shaped (Fig. 14.5b) QDs. In this partial excitonic emission spectrum, we find that the sequence of the following lines always obeys some “hard rules” [39],

$$X^- < XX^- < XX^0 < X^0. \quad (14.13)$$

The hard rules observed in all experimental spectra [25, 56, 60, 63, 64] are that (i) both X^- and XX^0 are red shifted with respect to X^0 (i.e., have positive binding energies) and (ii) the XX line always lies between X and X^- . Hard rule (iii) [39], related to X^{-2} , has not been measured yet for GaAs/AlGaAs QDs. These three hard rules plus the position of the X^0 line will provide the size of the base and the height of the QD [39]. From hard rules (i) and (ii) we estimate that the QDs seen in the optical spectroscopy measurement has a base diameter of 30–40 nm.

Interestingly, we find that the energetic relative position of the positive trion (X^+) is related to the QD shape. Figure 14.5a shows that in lens-shaped QDs the positive trion (X^+) is always redshifted with respect to neutral monoexciton

(X^0). In contrast to lens-shaped QDs, in Gaussian-shaped QDs (Fig. 14.5b) the X^+ has a transition from redshift to blueshift, when the QD height decreases, in agreement with experimental measurements [56]. Furthermore, our calculated transition energy $E_{X^0} = 1.758$ eV also agrees with the experimental value of 1.748 eV [56]. Thus, we conclude that Gaussian shape is more likely in droplet epitaxy-grown GaAs/AlGaAs QDs.

FSS of Mono-exciton vs. QD Shape. The FSS of an exciton [31, 66–68] refers to the splitting of the optical-allowed (bright) exciton states due to both intrinsic crystal asymmetry as well as external shape anisotropy. The role of these two factors has been often misconceived in the literature [56, 60, 63, 69], leading to the misuse of the FSS to infer shape anisotropy: In the Luttinger Hamiltonian representation, the effective mass of the hole is anisotropic in that its value along (100) is different from that along (110). Thus, if one ignores the fact that the QDs under consideration are made of an atomistically discrete material, the symmetry of circular-based QD in this Hamiltonian is C_{4v} . Despite this, numerous papers [25, 70] claimed that circular-based lens-shape QDs have D_{2d} symmetry. This is because in a continuum approximation the [110] and $[1\bar{1}0]$ directions are equivalent. In such a D_{2d} symmetry, the fourfold degenerate exciton (originating from an electron of $J_z = \pm 1/2$ and a heavy hole of $J_z = \pm 3/2$) splits into doubly degenerate bright state (Γ_5) and two nondegenerate dark states (Γ_1 and Γ_2 , respectively). Because Γ_5 is degenerate in this approximation, the FSS is zero for cylindrically symmetric QDs under the continuum point of view. To account for the observed nonzero FSS, the continuum theory assumes that the FSS originates, in its entirety, from deviations from cylindrical symmetry [56, 60, 63, 69]. This shape anisotropy (e.g., elongation in the $[1\bar{1}0]$ direction [56, 60, 63]) of the QD lowers the D_{2d} symmetry to C_{2v} . The doubly degenerate bright Γ_5 states splits into two nondegenerate states (Γ_2 and Γ_4 symmetry). The lifting of the degeneracy of the two bright exciton states is referred to as FSS and is used under the continuum point of view to fit the measured FSS into a geometric shape anisotropy. If the base center of the QD does not anchor on a common atom (namely, As atom in GaAs/AlGaAs), then the symmetry of the circular-based QD is C_1 , rather than C_{2v} . In the C_1 point group, the two bright exciton states belong to the same irreducible representation and they will couple, if their energy are close enough (namely $FSS < 5 \mu\text{eV}$ [68]). For QDs with $FSS > 5 \mu\text{eV}$, the FSS is not sensitive anymore to the choice of the QD base center.

In reality, the [110] and $[1\bar{1}0]$ directions are nonequivalent for QDs with zincblende crystal lattice. This leads to the fact that a QD with cylindrical shape does not have the commonly thought D_{2d} symmetry, but already has the lower C_{2v} symmetry. Thus, even a shape-symmetric QD has nonzero FSS. Although, this intrinsic crystal anisotropy was pointed out many times in atomistic theories [35, 45, 67], its contribution to the FSS has often been neglected by the community [56, 60, 63, 69]. Figure 14.6 shows the calculated atomistic many-body pseudopotential FSS for symmetric and asymmetric Gaussian-shaped QDs as well as symmetric lens-shaped QDs. In agreement with the atomistic point of view, we see that even the shape-symmetric Gaussian-shaped QD with base size of 30 nm has already a large FSS

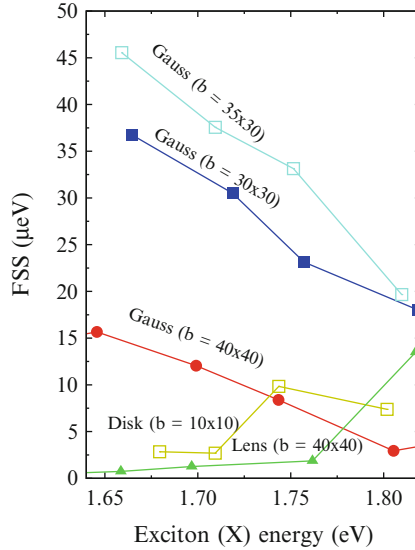


Fig. 14.6 FSS of neutral mono-excitons of GaAs/AlGaAs QDs as a function of exciton emission energy (QD height) for different shapes (symmetric lens shape, symmetric disk shape, and symmetric and asymmetric Gaussian shape) and base sizes (given in *parentheses* in nm). Taken from [41]. ©(2011) by the American Physical Society

($\sim 30 \mu\text{eV}$ for QDs having an exciton energy of 1.7 eV) and that shape asymmetry additionally adds some ($\sim 10 \mu\text{eV}$) FSS. Whereas, the increase of base size for the shape-symmetric QDs from 30 to 40 nm reduces the FSS by $\sim 20 \mu\text{eV}$. Thus, attributing all of the FSS to shape asymmetry will greatly exaggerate the shape asymmetry.

It is most interesting to note that the slope of the size-dependent FSS, for both symmetric and asymmetric Gaussian-shaped QDs, is opposite to the one seen in lens-shaped and in disk-shaped QDs. Specifically, the FSS of the Gaussian-shaped QDs decreases with increasing exciton emission energy (i.e., decreasing the QD height) in strong contrast to the case of lens-shaped and disk-shaped QDs, where the FSS increases with increasing exciton emission energy. We ascribe these two opposite size-dependent trends of the FSS to two competing effects: (i) FSSs will be enhanced by quantum confinement effect due to increased overlap of electron and hole wave functions; (ii) FSSs will be washed out by random AlGaAs alloy distribution due to an increased wave function leakage with decreasing QD height. Because the wave functions are expected to be more localized inside the QD (in the in-plane direction) in lens-shaped and disk-shaped QDs than in Gaussian-shaped QDs, the item (i) is dominant in lens-shaped and disk-shaped QDs. However, in Gaussian-shaped QDs, item (i) and (ii) are comparable. These factors explain the observed opposite trends. The calculated size-dependent trend of the FSS in Gaussian-shaped QDs is in excellent agreement with experimental measurements [60]. Thus, from the size-dependent trend of the FSS we suggest that droplet epitaxy-grown GaAs/AlGaAs QDs have a Gaussian shape.

In summary, we showed how the multi-exciton spectra of a droplet epitaxy QD encodes nontrivial structural information that can be uncovered by atomistic many-body pseudopotential calculations. We calculated single-particle energy levels, exciton gap, optical emission spectra, and FSSs for a large number of strain-free GaAs/AlGaAs QDs with three different shapes and different structure parameters (base size, height, and shape anisotropy). From such multi-exciton complex emission spectrum (“barcode”) and from the size-dependent trends of the FSS, we showed that the droplet epitaxy strain-free GaAs/AlGaAs QDs have a Gaussian shape, in agreement with XSTM measurements, but the previously determined QD height (~ 14 nm) as “seen” by XSTM [57, 62] could not possibly be consistent with the excitonic signature (1.7–1.9 eV) [25, 56, 56, 60, 63], as the latter must reflect a 1–4 nm tall QD. Both, spectroscopy and XSTM measurements, were done on GaAs QDs capped by an $\text{Al}_{0.3}\text{Ga}_{0.7}\text{As}$ barrier layer. The fact that XSTM sees tall QDs and spectroscopy sees flat QDs suggests that different QDs must have been investigated. Indeed, Koenraad and Takaaki clarified for us that the droplet QDs used in XSTM were different than those used for PL measurements. This approach therefore holds the promise that, with increasing spectral resolution and more multi-excitonic barcode lines, a detailed structural information could be revealed.

14.4 Influence of the Atomic-Scale Structure on the Exciton Fine-Structure Splitting in of QDs in a Vertical Electric Field

One of the leading proposals for the *on-demand* generation of polarization-entangled photons is the utilization of the cascade decay of biexciton–exciton–ground state [71] in semiconductor QDs [72], as illustrated schematically in Fig. 14.7a. A serious impediment to the success of this proposal is the existence of the FSS discussed previously, which must be suppressed below the radiative linewidth (≈ 1 μeV). The FSS is affected by the atomistic symmetry of the QD confining potentials [35, 73–77] and can be manipulated by strain [78, 79], lateral electric fields [80], vertical electric fields [19, 20, 81], magnetic field [82], and strong coherent lasers [83, 84]. A number of surprising puzzles surround the tuning of the FSS by a vertical electric field. First, it is predicted theoretically [68], and confirmed experimentally [19, 79] and theoretically [85], that for QDs made of random alloys (with symmetry lower than C_{2v}) the two bright components of the excitons undergo an *anticrossing* as a function of field applied along the $\{100\}$ or $\{110\}$ directions [68]. Second, since it has been established that the FSS is related to the atomistic in-plane asymmetry between the $[110]$ and $[1\bar{1}0]$ crystallographic directions, it would appear that such an intrinsic quantity would not lend itself to tuning via *vertical* field. Nevertheless, it was shown experimentally that the FSS can be tuned rather effectively in $\text{In}(\text{Ga})\text{As}/\text{GaAs}$ QDs by applying an electric field along the growth direction [19]. Third, the role of strain is unclear: while electric field control



Table 14.1 Sizes and compositions of different QDs investigated in this section

QD	Composition	Size (nm) a, b, h	Barrier (% Al)	
			Top	Bottom
Lens shape				
00	In _{0.8} Ga _{0.2} As	10, 7.5, 2.5	0	0
01	GaAs	45, 45, 3	35	35
02	GaAs	70, 50, 3	45	45
03	GaAs	70, 50, 3	35	45
04	GaAs	60, 40, 2	35	45
05	GaAs	25, 31, 3.9	35	35
Gaussian shape				
06	GaAs	30, 30, 3	30	30
07	GaAs	30, 30, 4	30	30
08	GaAs	30, 30, 6	30	30
09	GaAs	35, 30, 3	30	30
10	GaAs	35, 30, 4	30	30
11	GaAs	35, 30, 6	30	30
12	Al _{0.06} Ga _{0.94} As	30, 30, 3	30	30
13	Al _{0.06} Ga _{0.94} As	30, 30, 6	30	30
14	Al _{0.06} Ga _{0.94} As	35, 30, 3	30	30
15	Al _{0.06} Ga _{0.94} As	35, 30, 6	30	30

The sizes a , b , and h describe the elliptic axis along the [110] and $[1\bar{1}0]$ directions and the height, respectively. Taken from [21]. ©(2012) by the American Physical Society

We consider lens-shaped and Gaussian-shaped QDs with the properties (composition and geometry) given in Table 14.1. The atom positions are relaxed using the VFF method [46] and the single particle states are calculated using the atomistic empirical pseudopotential approach [43, 46] as outlined in Sect. 14.2. We apply an external electric field following [49]. The direct and exchange Coulomb interactions are calculated from the atomic wave functions, and the correlated excitonic states are calculated by the CI approach as shown in Sect. 14.2 using 12 electron and 12 hole states (spin included), thus accounting for correlations.

Before we present our numerical results, we introduce a mesoscopic simple model where the Hamiltonian is split into different components:

$$H = H_{C_{2v}} + \delta H_{C_1} + q_s Fz, \quad (14.14)$$

where q_s is the charge of a particle in band s , i.e., $-e(+e)$ for conduction (valence) bands, $H_{C_{2v}}$ is the Hamiltonian of the QD with C_{2v} point group symmetry, which must be supplemented by the deviation from this symmetry by the term δH_{C_1} . This latter term represents the random alloy present in the barrier and possible impurities inside the GaAs QD, as well as shape asymmetries. In the space of the two bright states $|1\rangle$ and $|2\rangle$ the Hamiltonian has a simple form:

$$H = \begin{pmatrix} E_1 + \delta E_1 + \gamma_1 F & s_0/2 \\ s_0/2 & E_2 + \delta E_2 + \gamma_2 F \end{pmatrix}. \quad (14.15)$$

The exciton energies of the high symmetric hypothetical structure given by $E_1 = \langle 1|H_{C_{2v}}|1\rangle$ and $E_2 = \langle 2|H_{C_{2v}}|2\rangle$ are different due mainly to strain [36] (nearly vanishing in the case of strain free GaAs QDs). The lowering of the symmetry to C_1 leads to the terms $\delta E_1 = \langle 1|\delta H_{C_1}|1\rangle$ and $\delta E_2 = \langle 2|\delta H_{C_1}|2\rangle$ and also to $s_0/2 = \langle 1|\delta H_{C_1}|2\rangle$ and $\gamma_i = \langle i|q_{sz}|i\rangle$. Redefining $E_1 + \delta E_1$ as E_0 and $\delta = E_2 - E_1 + \delta E_2 - \delta E_1$ and removing the linear term in the field from $|1\rangle$ leads to

$$H = \begin{pmatrix} E_0 & s_0/2 \\ s_0/2 & E_0 + \delta + (\gamma_2 - \gamma_1)F \end{pmatrix}, \quad (14.16)$$

which corresponds to the anticrossing model used by Bennett et al.[19]:

$$E \begin{pmatrix} \cos \theta \\ \sin \theta \end{pmatrix} = \begin{pmatrix} E_0 & s_0/2 \\ s_0/2 & E_0 - \gamma(F - F_0) \end{pmatrix} \begin{pmatrix} \cos \theta \\ \sin \theta \end{pmatrix}. \quad (14.17)$$

We identify $\gamma = \gamma_1 - \gamma_2$ and $\gamma F_0 = \delta$ from Eqs.(14.15) and (14.17). This simple reformulation clarifies the origin of the terms:

- γ represents the difference in the response of $|1\rangle$ and $|2\rangle$ to the applied field and γF_0 the intrinsic FSS due to the inequivalence of $[110]$ and $[1\bar{1}0]$ in C_{2v} (small for a strain-free structure) and the lowering to C_1 symmetry through atomistic alloy effects.
- s_0 is the FSS at the anticrossing and quantifies the coupling between the bright states. In a pure GaAs QD embedded in a pure AlAs matrix, the bright states are expected to cross [68] due to the high C_{2v} symmetry of the structure and $s_0 = 0$. However, the reduction of the QD symmetry due to the alloy fluctuations in the AlGaAs barrier at the QD interface leads to an avoided crossing [68] with $s_0/2 \neq 0$.
- F_0 is the field at the anticrossing. As the field approaches F_0 , the exciton eigenstates become a coherent mixture with components $\sin \theta$ and $\cos \theta$, where θ is the angle describing the orientation of the lowest eigenstate relative to the $[110]$ crystal axis.

The solution of Eq. (14.17) yields the eigenvalues (E_{\pm}) and angles [19]:

$$E_{\pm} = E_0 - \frac{\gamma(F - F_0)}{2} \pm \frac{1}{2} \sqrt{\gamma^2(F - F_0)^2 + s_0^2} \quad (14.18)$$

$$\theta = \pm \tan^{-1} \left[\frac{s_0}{\gamma(F - F_0) \pm (E_- - E_+)} \right]. \quad (14.19)$$

We note at this point that the model of Eq.(14.15) does not include any field dependence of the off-diagonal terms. Such terms would lead to an additional

Table 14.2 Transition energy E_0 and FSS parameters defined in Eq. (14.17) and extracted from our numerical results

QD	E_0 (meV)	s_0 (μeV)	γ ($\mu\text{eV cm/kV}$)	F_0 (kV/cm)
00	1363	?	0.15	+ 273
01	1644	0.1	0.11	+17
02	1650	0.1	0.08	-48
03	1643	0.1	0.08	-48
04	1742	0.9	0.14	-43
05	1679	0.3	0.33	+29
06	1762 ± 2	0.8 ± 0.3	0.85 ± 0.08	-21 ± 5
07	1718 ± 2	0.4 ± 0.1	0.95 ± 0.06	-26 ± 3
08	1666 ± 1	0.9 ± 0.8	1.06 ± 0.07	-25 ± 2
09	1754	0.9	0.79	-33.5
10	1714	0.4	0.78	-37.4
11	1660	0.7	0.96	-40.5
12	1806 ± 5	1.2 ± 0.7	0.74 ± 0.11	-14 ± 7
13	1727 ± 2	1.2 ± 0.5	0.85 ± 0.09	-15 ± 9
14	1799 ± 2	1.3 ± 1.0	0.73 ± 0.03	-25 ± 6
15	1721 ± 2	1.8 ± 1.4	0.84 ± 0.07	-40 ± 5

The error bars represent the range of parameters we obtain by running five different random alloy realizations (see Fig. 14.9). Taken from [21]. ©(2012) by the American Physical Society

coupling of the two bright states and could be used to tune the FSS through zero (if it would exactly compensate $s_0/2$). In our case of vertical field, this coupling is negligible, but in the case of a field with a component along a low symmetry direction (any direction but $[110]$ or $[1\bar{1}0]$) this term should exist. A future investigation of this effect would be worthwhile.

We first present our results for the strained $\text{In}_{0.8}\text{Ga}_{0.2}\text{As}$ QD00 (see Table 14.1) an emission energy that fits the measured results of Bennett et al. [19] very well. Figure 14.7 shows the Stark shift, FSS, and the oscillator strength as a function of vertical electric field.

We obtain a nearly linear change in the FSS with the E field in agreement with the experimental results [19]. A fit of our numerical results to the model of Eq. (14.17) yields the parameters given in Table 14.2. For the field dependence of the FSS, γ , we obtain a value of $0.15 \mu\text{eV cm/kV}$, somewhat lower than the value of $0.28 \mu\text{eV cm/kV}$ reported by Bennett et al. [19]. The strong shape and size dependence of the slope can explain this discrepancy and will be illustrated below. Our results for the set of strain-free GaAs QDs given in Table 14.1 are shown in Figs. 14.8 and 14.9, where we plotted the Stark shift, the FSSs, the polarization angle θ , and the oscillator strength as a function of the vertical E field. The results of the fit to the model of Eq. (14.17) are given in Table 14.2. We make the following observations.

FSS and Polarization Angle. The anticrossing described by Eq. (14.17) can be seen in Figs. 14.8c and 14.9 as a reduction of the FSS until the value s_0 , followed by an increase. The anticrossing is accompanied by a rotation of the polarization angle of

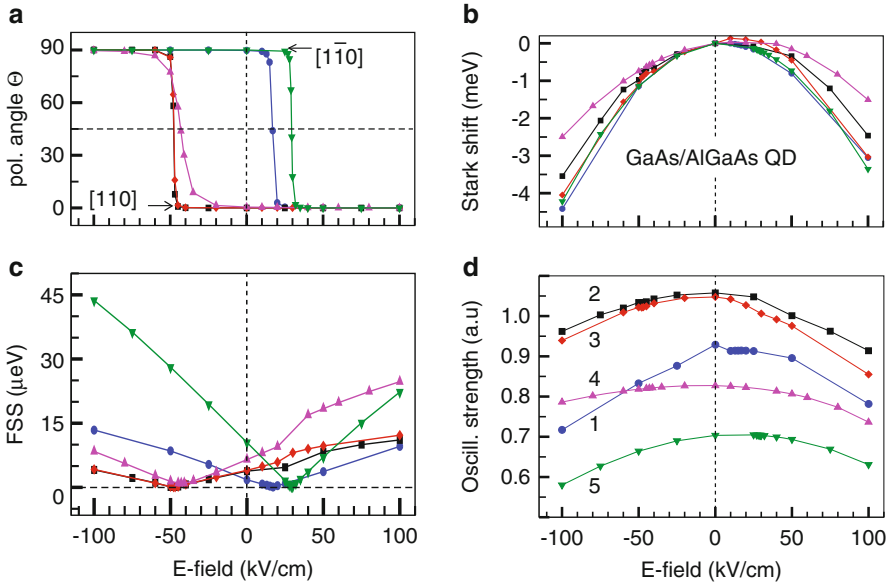


Fig. 14.8 Results for GaAs/AlGaAs strain-free QDs. (a) Polarization angle θ , (b) stark shift, (c) FSS, and (d) sum of intensities along the $[110]$ and the $[\bar{1}\bar{1}0]$ crystal directions as a function of applied vertical E field. The circles, squares, diamonds, up-triangles, and down-triangles are for the QD01, QD02, QD03, QD04, and QD05, respectively. Taken from [21]. ©(2012) by the American Physical Society

the lowest energy exciton state [68], as shown in Fig. 14.8a. At the field F_0 , where the anticrossing occurs, the polarization angle changes more rapidly when s_0 is small in agreement with the model.

Shape and Size Effects on the Tunability γ . Table 14.2 reveals that γ increases with the height of the QDs: tall QDs are more tunable in the vertical electric field, which correlated with the polarizability of the exciton states. Comparing QD05 and QD07 with similar dimensions but different shapes shows that Gaussian-shaped QDs have a larger γ value.

Shape and Size Effects on s_0 . From Table 14.2 we conclude that the shape effect on s_0 is rather moderate, while the size effect shows a trend for larger values of s_0 in larger QDs. This latter trend is, however, overshadowed by a very strong random alloy effect (see next).

Random Alloy Effects on s_0 and F_0 . In Fig. 14.9a–c we generated the same QD structure with different random realizations of the barrier material. In Fig. 14.9e–g the QDs have a 6% Al content and these Al atoms are randomly distributed in five different realizations within the QDs. These variations represent fluctuations that should be encountered experimentally. We notice that both s_0 and F_0 are significantly affected by these atomistic effects. For instance, the pure GaAs QD

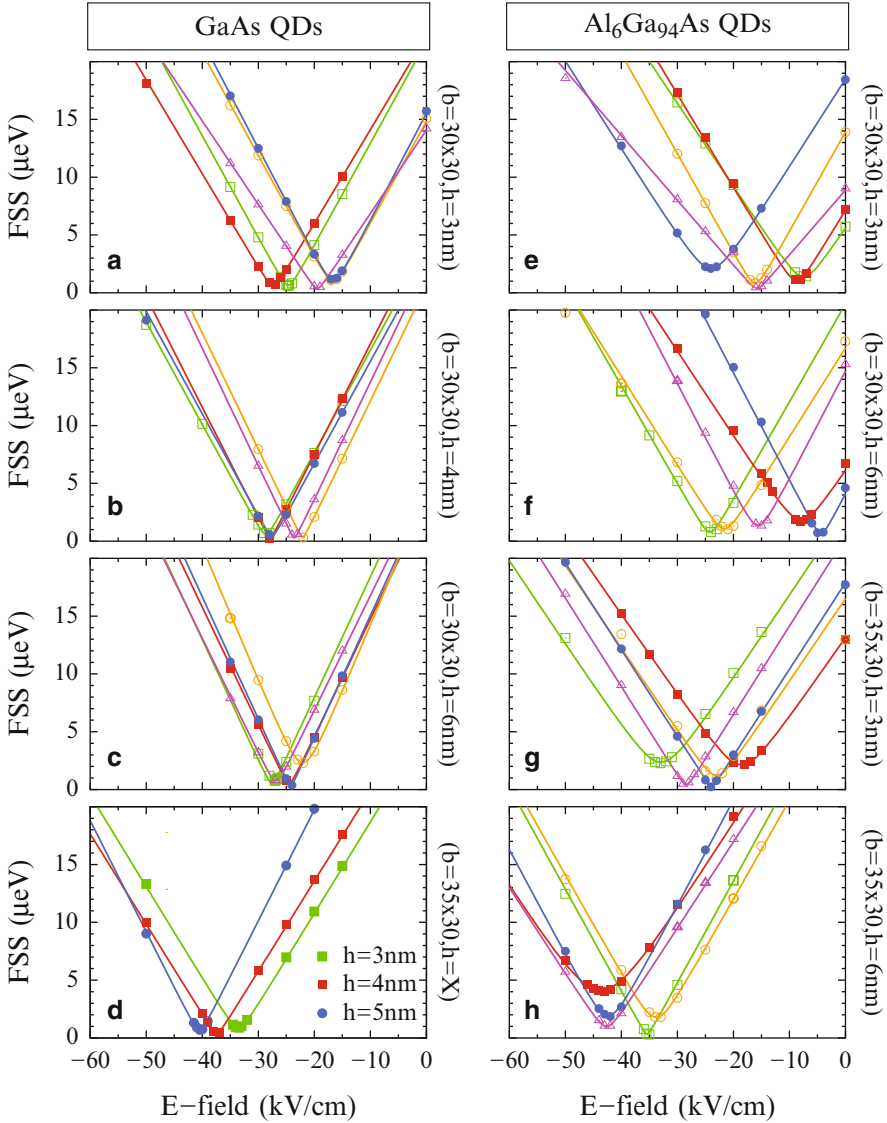


Fig. 14.9 FSS as a function of the electric field for various QDs listed in Table 14.1. Five different alloy configurations of the $\text{Al}_{30}\text{Ga}_{70}\text{As}$ matrix have been used in (a)–(c) and five different QD alloy configurations in (e)–(h). Taken from [21]. ©(2012) by the American Physical Society

QD08 can exist with s_0 of 0.1 or 1.7 μeV by merely changing the realization (i.e., the random distribution of the cations) of the barrier material. Furthermore, QD15 can exist with s_0 of 0.4 or 3.2 μeV by changing the random distribution of the 6%Al atoms inside the QD. The sensitivity of s_0 and F_0 on the alloy realization

is in agreement with our model (Eq. (14.15)), where these terms have been shown to originate from the lowering of the symmetry (term δH_{C1}).

Random Alloy Effect on γ . The value of γ is only weakly dependent on the details of the alloy realization (see Fig. 14.9) but rather strongly on the QDs geometry, size, and composition (see Fig. 14.8c). Indeed, following our model, γ gives the difference in the response of $|1\rangle$ and $|2\rangle$ to the applied field and is directly related to the light-hole component of the exciton state. For a pure heavy-hole exciton, γ vanishes. The light-hole component does change significantly for different shapes (QD01, QD02, QD03, QD04, and QD05 have 3.5%, 2.4%, 2.6%, 5.0%, and 8.2%, light-hole component, respectively) but remains constant for different alloy realizations.

Oscillator Strength. Figure 14.8d shows a moderate change of the oscillator strength, in the range of 10%, with varying E field in the range of -100 to $+100$ kV/cm.

How to Select QDs with Small s_0 . Our present work shows not only that GaAs QDs are good candidates to achieve small FSS via vertical electric field but also that rather large fluctuations of s_0 should be expected within one homogenous set of QDs (that differ only by random alloy effects and have the same shape, size and composition). A selection of appropriate QDs (as practiced experimentally [87, 88]) will therefore be advantageous, if not necessary. From Eqs. (14.18) and (14.19) at zero field ($F = 0$) we can derive the following expressions:

$$F_0 = \frac{\Delta E \cos 2\theta}{\gamma} \quad ; \quad s_0 = -\Delta E \sin 2\theta, \quad (14.20)$$

where ΔE is the FSS at $F = 0$. Interestingly, s_0 does not depend on the slope γ and only requires a single measurement of the FSS and the corresponding polarization angle θ at zero field. We have used Eq. (14.20) in Table 14.2 to report our value of F_0 for QD00. For the value of s_0 , however, if ΔE is large, a small inaccuracy in the measurement, or the calculation in our case, of the angle θ will lead to an inaccurate determination of s_0 . With a ΔE of $50 \mu\text{eV}$ and an angle accuracy of 2° we obtain s_0 with an error bar of $\pm 3.5 \mu\text{eV}$, which is too large to be useful. However, Eq. (14.20) is very useful for QDs where ΔE is not too large, which represent the QDs that will require weaker E fields to be tuned.

In summary, we showed that the FSS in GaAs/AlGaAs and InGaAs/GaAs self-assembled QDs can be effectively tuned by a vertical electric field. Indeed, the tuning rate for GaAs QDs is between 0.1 and $1 \mu\text{eV cm/kV}$, depending on size and geometry, and is surprisingly similar to the tuning rate obtained with lateral electric fields ($0.15 \mu\text{eV cm/kV}$ [89]). Our results for InGaAs QDs are in good agreement with experiment, while the results for GaAs QDs represent predictions. The minimum FSS, s_0 , for GaAs QDs, is between 0.1 and $1.8 \mu\text{eV}$, depending on size and geometry. However, alloy fluctuations in the surrounding barrier lead to a variations of s_0 in the range of $\pm 1.4 \mu\text{eV}$ calling for a postselection of the “best QDs,” for which we suggest a simple experimental procedure requiring only one measurement at zero field.

This dependence of s_0 , and also F_0 , on the random atomic arrangement is in agreement with the expectations from a simple mesoscopic model that shows these terms to be proportional to the “amount of deviation from C_{2v} ” symmetry toward the lower C_1 symmetry. Hence, a QD made of a random alloy (with formally C_1 symmetry) with an atomic decoration of the lattice that will *resemble* the C_{2v} symmetry, will have the smallest s_0 . This represents a striking example of an observable, where the conventional treatment of a random alloy through a replacement of the atomic distribution by an average (VCA [90]) or an effective medium (CPA [90]) fails. In this case, the position of each and every atom in a structure made of several thousand atoms is relevant.

As we mentioned above, the FSS can be tuned to zero in the case of vertical electric field plus a component of field along a low symmetry direction (any direction but [110] or $[1\bar{1}0]$). Because the model of Eq.(14.15) under a single vertical field does not include any field dependence of the off-diagonal terms, an additional field giving rise to field-dependent terms to the off-diagonal terms can be used to compensate field-independent terms and then tune the FSS to zero. Indeed, it was demonstrated in a recent experiment [91] in InGaAs/GaAs QDs, where in addition to vertical electric field a field of anisotropic biaxial strain delivered by piezoelectric actuators was applied in the (001) plane. However, our finding of the significant influence of random alloy fluctuations in both QD and barrier on the values of minimum FSS s_0 and F_0 show that tuning several QDs to the optimum properties in the same sample is unlikely. The realization of large arrays of QD entanglement sources [92] would therefore require a receipt to suppress the alloy randomness, which is certainly a formidable challenge. Thus, the alloy randomness will prevent us to integrate large number of entanglement sources into one chip.

14.5 HH–LH Mixing in Semiconductor QDs

HH–LH mixing occurs only when states derived from bulk HH band and from bulk LH band, respectively, belong to the same irreducible representation of the point group in a nanostructure. The point group of self-assembled QDs on (001) substrates are often mis-assigned to be D_{2d} [23, 25, 70, 93], because the QD shape resembles a lens or a truncated cone with a circular base [39] and the in-plane [110] and $[1\bar{1}0]$ directions are incorrectly considered to be equivalent. The underlying bulk HH and LH bands at the Γ -point (Γ_8 in bulk T_d symmetry) transform to two *different* representations Γ_7 and Γ_6 in the D_{2d} point group [94], and therefore HH–LH mixing is expected to be forbidden in QDs. The experimentally observed HH–LH mixing in self-assemble In(Ga)As/GaAs [24] and CdTe/ZnTe [23] QDs were thus attributed to strain, which was assumed to deform the QD symmetry from D_{2d} to C_{2v} . In this scenario, HH–LH mixing is allowed since both HH and LH transform to the *same* representation Γ_5 of C_{2v} . HH–LH mixing is proportional to the magnitude of shear strain components (described by the off-diagonal terms of the Pikus–Bir Hamiltonian [12, 13]). One therefore expects HH–LH mixing to vanish in strain-free QDs. However, large HH–LH mixing was recently observed experimentally

in strain-free GaAs/AlGaAs QDs grown by molecular droplet epitaxy [4, 86]. The anisotropic QD geometric shape, which also lowers the QD symmetry from D_{2d} to C_{2v} , is alone considered as the origin of this unexpected HH–LH mixing [25].

In reality, the atomistic symmetry of ideal circular-based lens-shape or Gaussian-shape QDs is already C_{2v} , because the [110] and $[1\bar{1}0]$ directions are nonequivalent. This is unlike T_d zinc-blende crystal and D_{2d} symmetric (001) quantum well (QW), where the [110] direction is identical to the $[1\bar{1}0]$ direction with S_4 operations i.e., 90° rotation followed with reflection through a (001) mirror plane [94]. *HH–LH mixing is consequently intrinsically allowed in self-assembled QDs even without built-in strain or QD shape anisotropy.* Furthermore, HH–LH mixing was found earlier even for $k = 0$, in D_{2d} QWs [95–97] and assigned to stem from C_{2v} interfaces [98, 99] since HH–LH mixing is allowed under local microscopic point group C_{2v} . The k-linear terms, originating from Rashba and Dresselhaus spin–orbit interactions, existing as off-diagonal terms in bulk valence band Luttinger–Kohn [100] or Kane [101] Hamiltonians, can also induce HH–LH mixing in QDs as a result of quantum confinement [22, 99, 102]. Fischer and Loss [22] and Tanaka et al. [102] studied HH–LH mixing in strain-free QDs taking account of the mechanism of the bulk linear terms alone. We notice that the alloy randomness in the QDs or barrier further lowers the QD symmetry and thus enhances HH–LH mixing. In summary, there are six mechanisms discussed in connection to HH–LH mixing in QD: (i) built-in shear strain [23, 24]; (ii) QD shape anisotropy [25]; (iii) intrinsic nonequivalence of the [110] and $[1\bar{1}0]$ directions; (iv) low local microscopic symmetry of the interfaces [49, 98, 99]; (v) bulk k-linear terms [22, 99, 102]; and (vi) alloy randomness in the QD or barrier, which was often neglected. To the best of our knowledge, the relative importance of these six HH–LH mixing mechanisms in QDs has yet to be addressed.

In this section a comprehensive and quantitative analysis of the aforementioned mechanisms is given using the atomistic empirical pseudopotential method [43, 46, 47] for both strain-free GaAs/Al(Ga)As and strained In(Ga)As/GaAs QDs with various shapes and sizes. We find that in strain-free nominal C_{2v} GaAs QDs (the nominal point group defines the QD symmetry, neglecting the symmetry breaking by alloy randomness), mechanisms (iii) (intrinsic nonequivalence of the [110] and $[1\bar{1}0]$ directions) and (iv) (interface effects) contribute 60% and 40%, respectively, to the HH–LH mixing. In strained In(Ga)As/GaAs QDs, mechanism (i) (built-in shear strain) provides 80% of the HH–LH mixing and the remaining 20% originate from mechanisms (iii) and (iv) in the ratio 3:2. Most interestingly we discover a quantum chain mediated by QD intermediate states that effectively brings the ground state of bulk LH band closer in energy to the ground state of bulk HH band and then enhances the HH–LH mixing. We refer this phenomena to quantum transmissibility of the HH–LH mixing.

The bulk band character of the QD states is gained by projection onto the bulk $\text{HH} = |3/2, \pm 3/2\rangle$, $\text{LH} = |3/2, \pm 1/2\rangle$, and spin–orbit split (SO) = $|1/2, \pm 1/2\rangle$ bands. However, all available HH–LH mixing mechanisms blend together in the QD states and prevent them to be accessed individually. We develop a formula, based on perturbation theory, to isolate the impact of the aforementioned mechanisms onto

the HH–LH mixing of the QD ground hole state h_0 . Specifically, we separate the QD Hamiltonian into two parts: $H = H_0 + \delta V$, where H_0 is the QD Hamiltonian without HH–LH mixing producing unperturbed QD ground states derived from bulk HH and LH bands: $\Psi_{\text{HH}}^0 = |u_{\text{HH}}; \phi_{\text{HH}}^0\rangle$ and $\Psi_{\text{LH}}^0 = |u_{\text{LH}}; \phi_{\text{LH}}^0\rangle$, respectively, where $|u_{\text{HH}}\rangle$ and $|u_{\text{LH}}\rangle$ are bulk Bloch functions and ϕ_i^0 are the envelop functions associated with the bulk band i . The perturbative potential is $\delta V = \delta V_{(i)} + \delta V_{(ii)} + \delta V_{(iii)} + \delta V_{(iv)} + \delta V_{(v)} + \delta V_{(vi)}$, accounting for the six HH–LH mixing mechanisms (i)–(vi), respectively. δV couples unperturbed QD states. The perturbed QD ground state h_0 , with dominant bulk HH character, can now be evaluated by a perturbation expansion [18, 22, 23]:

$$|\Psi_{h_0}\rangle = \lambda_{\text{HH}}|\Psi_{\text{HH}}^0\rangle + \lambda_{\text{LH}}|\Psi_{\text{LH}}^0\rangle + \dots, \quad (14.21)$$

where λ_{LH} is a mixing coefficient given by

$$\lambda_{\text{LH}} = \langle \Psi_{\text{LH}}^0 | \delta V | \Psi_{\text{HH}}^0 \rangle / \Delta_{\text{HL}}^0, \quad (14.22)$$

λ_{HH} is a renormalization factor and Δ_{LH}^0 is the energy splitting between $|\Psi_{\text{HH}}^0\rangle$ and $|\Psi_{\text{LH}}^0\rangle$. The numerator of Eq. (14.22) is the HH–LH coupling matrix element $\delta V_{\text{HL}} = \langle \Psi_{\text{LH}}^0 | \delta V | \Psi_{\text{HH}}^0 \rangle$ which can be inferred (as shown in Fig. 14.10) by fitting the bulk LH character of h_0 to Eq. (14.22). Δ_{HL}^0 is approximated by the energy splitting Δ_{HL} of the highest HH- and highest LH-dominated QD hole states. The relative importance of the HH–LH mixing mechanism γ for a QD is obtained from the ratio of $\delta V_{\gamma, \text{HL}}$ to δV_{HL} , where $\delta V_{\gamma, \text{HL}} = \langle \Psi_{\text{LH}}^0 | \delta V_{\gamma} | \Psi_{\text{HH}}^0 \rangle$ is the component of HH–LH coupling matrix originating from mechanism γ . The challenge is how to isolate $\delta V_{\gamma, \text{HL}}$, $\gamma = (i), \dots, (vi)$, from the overall δV_{HL} . In the following we extract each $\delta V_{\gamma, \text{HL}}$ using a comparative study approach through the design of different types of QDs.

Mechanism (i) Built-In Nonuniform Strain. The lattice-mismatch-induced strain, which has a significant impact on the electronic properties of strained QDs, is the main difference between strained In(Ga)As/GaAs QDs and strain-free GaAs/AlGaAs QDs. Figure 14.3b shows that the built-in biaxial strain [12, 13] splits the bulk InAs HH and LH bands by as much as 0.18 eV in an In(Ga)As/GaAs QD, otherwise bulk HH and LH bands are degenerate, as shown in Fig. 14.3a for a strain-free GaAs/AlAs QD. As mentioned above, the magnitude of the HH–LH mixing is proportional to shear strain components as they are present in the off-diagonal terms of the Pikus–Bir Hamiltonian [12, 13]. Figure 14.10 shows the LH character λ_{LH}^2 of the h_0 state (represented as Δ) as a function of Δ_{HL} for 24 nominal C_{2v} lens-shape or Gaussian-shape GaAs/Al(Ga)As QDs with height varying from 2 to 7 nm. The corresponding base sizes are listed in Table 14.3. Here, nominal refers to symmetry excluding alloying effect. Despite different shapes, sizes, and barrier compositions, λ_{LH}^2 of all QDs, except QD #3, fall on the blue line described by Eq. (14.22) with an overall HH–LH coupling matrix element $\delta V_{\text{HL}} = 2.15$ meV. The single value of δV_{HL} for all GaAs QDs illustrates the negligible contribution of the QD height and QD shape to δV_{HL} for C_{2v} symmetry QDs. The LH character

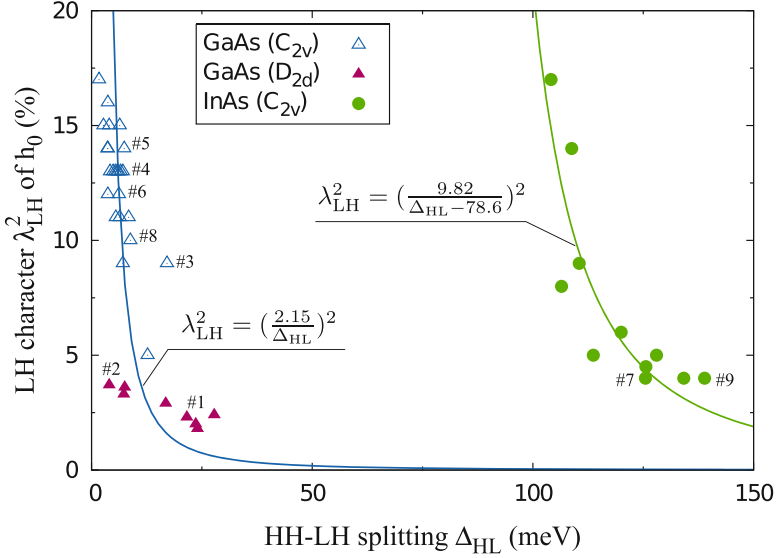


Fig. 14.10 Bulk LH character λ_{LH}^2 of QD ground hole state h_0 as a function of HH–LH splitting Δ_{HL} for nominal C_{2v} lens-shape and Gaussian-shape GaAs/Al(Ga)As, lens-shaped In(Ga)As/GaAs, and nominal D_{2d} disk-shaped GaAs/Al(Ga)As QDs. The *numbering* of the QDs corresponds to the numbers in Table 14.3, which gives QD geometry properties and more detailed results, except #8 and #9 which correspond to the QDs shown and described in Fig. 14.2

λ_{LH}^2 of 11 nominal C_{2v} lens-shaped In(Ga)As/GaAs QDs with varying QD height from 2 to 6 nm are shown by green dots in Fig. 14.10. In contrast to GaAs QDs, the value of λ_{LH}^2 of In(Ga)As QDs can not be described by Eq. (14.22) using a single δV_{HL} value. Surprisingly, if one subtracts $\delta E_{\text{HL}} = 78.6$ meV from Δ_{HL} , then all data points lie around a curve (green line in Fig. 14.10) given by Eq. (14.22) with $\delta V_{\text{HL}} = 9.82$ meV. The enhancement of the HH–LH coupling matrix element δV_{HL} from 2.15 meV for strain-free GaAs QD to 9.82 meV for strained In(Ga)As QDs exclusively arises from the built-in nonuniform strain. We therefore conclude that the mechanism of built-in strain contributes around 80% to the HH–LH mixing since $\delta V_{(i),\text{HL}}/\delta V_{\text{HL}} = 0.78$ in strained In(Ga)As/GaAs QDs.

Quantum Transmissibility of HH–LH Mixing in QDs. The “red shift” δE_{HL} of the effective HH–LH splitting ($\Delta_{\text{HL}} - \delta E_{\text{HL}}$) required to fit the data in strained In(Ga)As/GaAs QDs arises from the effect of intermediate QD states energetically located between the HH and LH two ground states $|\Psi_{\text{HH}}^0\rangle$ and $|\Psi_{\text{LH}}^0\rangle$. In strained In(Ga)As/GaAs QDs there are tens of intermediate QD states derived from the bulk HH band between $|\Psi_{\text{HH}}^0\rangle$ and $|\Psi_{\text{LH}}^0\rangle$. This is a consequence of the large splitting between bulk HH and LH bands (shown in Fig. 14.3) induced by built-in strain. The direct coupling between $|\Psi_{\text{HH}}^0\rangle$ and $|\Psi_{\text{LH}}^0\rangle$ is expect to be very small since it is inversely proportional to Δ_{HL} (Eq. (14.22)). However, the unperturbed LH ground state $|\Psi_{\text{LH}}^0\rangle$ in a QD can strongly mix with its nearest HH-dominated QD states and

Table 14.3 Bulk band (HH, LH, and SO) characters of the highest three hole states h_0 , h_1 , and h_2 for strain-free GaAs/Al(Ga)As and strained $\text{In}_{0.6}\text{Ga}_{0.4}\text{As}/\text{GaAs}$ QDs

QD	Shape cylindrical Composition	Point group	HH/LH/SO (%)		
			$E(h_0)$	$E(h_1)$	$E(h_2)$
#1	Cylindrical	D_{2d}	96/2/0	92/5/0	92/5/1
	GaAs/AlAs		0.0	-8.1	-8.6
#2	Gaussian	$C_1(D_{2d})$	95/4/0	42/57/0	15/84/0
	GaAs/AlGaAs		0.0	-2.8	-4.0
#3	Gaussian	C_{2v}	87/9/1	54/42/2	43/52/2
	GaAs/AlAs		0.0	-3.2	-7.1
#4	Gaussian	$C_1(C_{2v})$	85/13/0	34/64/0	47/51/0
	GaAs/AlGaAs		0.0	-7.1	-10.3
#5	Elong. [1 $\bar{1}$ 0]	$C_1(C_{2v})$	85/14/0	37/61/0	49/49/0
	GaAs/AlGaAs		0.0	-7.3	-10.1
#6	Elong. [110]	$C_1(C_{2v})$	87/12/0	34/64/0	44/54/0
	GaAs/AlGaAs		0.0	-6.2	-9.7
#7	Lens	$C_1(C_{2v})$	94/4/0	89/8/1	89/8/1
	InGaAs/GaAs		0.0	-12.1	-17.2

The Ga composition in the AlGaAs alloy barrier is 70%. All QDs have a height of 3 nm. The base size is 25.2 nm for both disk-shape and lens-shaped QDs. The base size is 30 nm and 35×30 nm for circular (#3 and #4) and elongated (#5 and #6) Gaussian-shape QDs, respectively. The energy levels (in meV) of h_1 and h_2 with respect to h_0 are also given beneath the bulk band character of each QD. The point group in parentheses is the symmetry of the QD without considering alloy randomness

these states increase the LH character of their own nearest HH-dominated QD states and eventually brings LH character to $|\Psi_{\text{HH}}^0\rangle$. This process forms a transmission chain for HH–LH mixing. We refer to this enhancement of the HH–LH mixing mediated by intermediate QD states as quantum transmissibility of the HH–LH mixing. This quantum transmissibility is further confirmed by the special point (QD #3) of a nominal C_{2v} GaAs QD in Fig. 14.10. In its QD family, the impact of quantum transmissibility of HH–LH mixing is exclusively acting on QD #3 because its $h_0 \approx |\Psi_{\text{HH}}^0\rangle$ and $h_2 \approx |\Psi_{\text{LH}}^0\rangle$ are mediated by a HH-dominated QD state (h_1) (as shown in Table 14.3), whereas in the remaining QDs of this family the state $h_0 \approx |\Psi_{\text{HH}}^0\rangle$ is immediately followed by $h_1 \approx |\Psi_{\text{LH}}^0\rangle$. Surprisingly, the redshift energy δE_{HL} modifying the HH–LH splitting with respect to the bare HH–LH splitting is universal for one QD family, e.g. $\Delta_{\text{HL}} - 78.6$ meV, for a family of nominal C_{2v} In(Ga)As/GaAs QDs. To the best of our knowledge, this novel quantum transmissibility of HH–LH mixing in QDs is discovered and quantitatively analyzed here for the first time.

Mechanism (vi) Effect of Alloy Randomness in the Barrier or Inside the QD. Its negligible contribution to HH–LH mixing in QDs ($\delta V_{(\text{vi}),\text{HL}} \sim 0$) is exhibited by the fact that (shown in Fig. 14.10) both InAs/GaAs and $\text{In}_{60}\text{Ga}_{40}\text{As}/\text{GaAs}$ QDs and

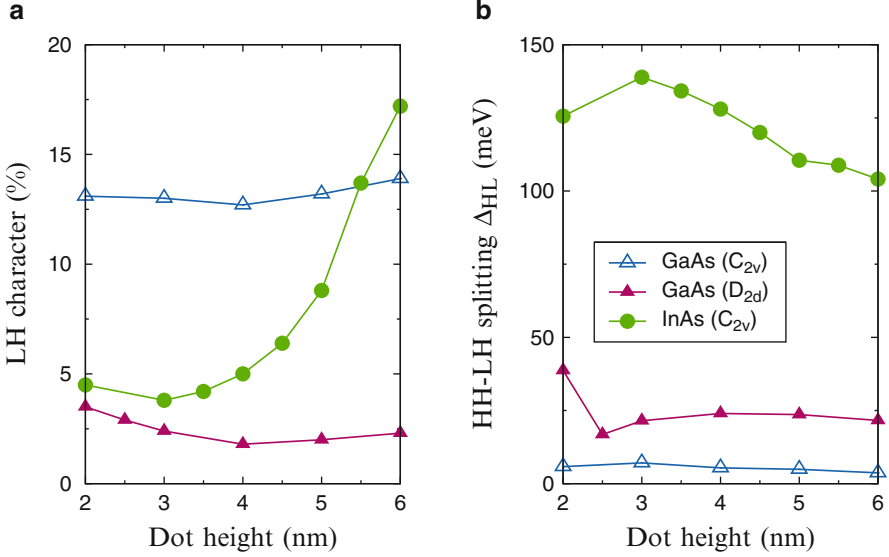


Fig. 14.11 (a) LH character of QD ground hole state h_0 and (b) HH-LH splitting Δ_{HL} as a function of QD height for nominal D_{2d} and C_{2v} GaAs/Al(Ga)As QDs and nominal C_{2v} In(Ga)As/GaAs QDs

both GaAs/AlAs and GaAs/AlGaAs QDs share an overall HH-LH coupling matrix element $\delta V_{HL} = 9.82$ meV and 2.15 meV, respectively. A further analysis of alloy effects is done via studying λ_{LH}^2 variation induced by fluctuations in the random atomic configuration. These atomic fluctuations have a significant effect on both FSS [21] and optical polarization [39] in QDs. Five random atomic configurations of the alloy barrier for a Gaussian-shape 3 nm height GaAs/Al₃₀Ga₇₀As QD lead to $\lambda_{LH}^2 = 13.3, 13.0, 12.9, 13.1, 12.8\%$, with a standard deviation $\sigma = 0.2\%$. Meanwhile, five random atomic configurations of a In₆₀Ga₄₀As/GaAs alloy QD with 3 nm height give rise to four $\lambda_{LH}^2 = 3.6\%$ and one $\lambda_{LH}^2 = 3.8\%$. Our assertion of negligible alloy effect on HH-LH mixing is well supported by these results.

Mechanism (v) Bulk k-Linear Terms. Fischer and Loss [22] considered this mechanism as the only origin of HH-LH mixing in strain-free QDs and derived $\lambda_{LH} = \sqrt{3}\beta_{HL}\gamma_3/(2\sqrt{2}\gamma_2) \times a_z L/(L^2 - a_z^2)$ for a strain-free QD of base size L and QD height a_z , where $\gamma_{2,3}$ are Luttinger parameters and β_{HL} accounts for the difference in effective masses between the bands. For flat GaAs QDs ($a_z \ll L$), $\lambda_{LH} \simeq 0.53a_z/L$ [22] is linear proportional to the QD height a_z for fixed base size L . However, using atomistic pseudopotentials we find that λ_{LH}^2 of both D_{2d} disk-shaped and C_{2v} lens-shaped GaAs/Al(Ga)As flat QDs (shown in Fig. 14.11a) to be nonmonotonic with a weak dependence on QD height. This marked difference to the model of Fischer and Loss [22] demonstrates the negligible impact of bulk k linear terms on HH-LH mixing in flat QDs.

Mechanism (iv) Low Local Microscopic Symmetry Interfaces. The impact of local atomic symmetry of C_{2v} interface on HH–LH mixing was first proposed by Ivchenko et al. [98, 99] using phenomenological Hamiltonian to explain unexpected HH–LH mixing observed in D_{2d} GaAs/AlAs QWs [95–97]. The filled triangles in Fig. 14.10 show that the LH character λ_{LH}^2 of disk-shaped nominal D_{2d} GaAs QDs embedded in AlAs and $\text{Al}_{0.3}\text{Ga}_{0.7}\text{As}$ barriers can be fitted by the functions $[0.8/(\Delta_{\text{HL}} - 13)]^2$ and $(0.8/\Delta_{\text{HL}})^2$, respectively. Quantum transmissibility of HH–LH mixing plays again an important role in D_{2d} GaAs/AlAs QDs giving rise to a redshift of 13 meV in the effective HH–LH splitting. Table 14.3 shows that the confinement potential of the AlAs barrier is so large that additional QD states exist between the two QD ground hole states of $|\Psi_{\text{HH}}^0\rangle$ and $|\Psi_{\text{LH}}^0\rangle$ in D_{2d} GaAs/AlAs QDs. No such intermediate states exist in QDs embedded in $\text{Al}_{0.3}\text{Ga}_{0.7}\text{As}$. The low local atomic symmetry interfaces induce a HH–LH coupling $\delta V_{(\text{iv}),\text{HL}} = 0.8$ meV. Moreover, the barrier composition independence of $\delta V_{(\text{iv}),\text{HL}} = 0.8$ meV further confirms the negligible contribution of alloy randomness effect onto the HH–LH mixing.

Mechanism (ii) QD Shape Anisotropy. Seven out of the 24 nominal C_{2v} GaAs QDs have an anisotropic shape: 6 QDs are elongation along the $[1\bar{1}0]$ direction and one along the $[110]$ direction, having base size of 35×30 nm and various heights. The LH character λ_{LH}^2 of seven irregular QDs, together with 17 circular-based QDs, fall on a single curve (shown in Fig. 14.10) indicating the minor contribution of the QD shape anisotropy to the HH–LH mixing. Specifically, the LH characters are $\lambda_{\text{LH}}^2 = 14, 13,$ and 12% for QDs elongated along the $[1\bar{1}0]$ direction (QD #5), with a circular base (QD #4), and elongated along $[110]$ (QD #6), respectively. Mechanism (ii) induces a HH–LH mixing with magnitude $\delta V_{(\text{ii}),\text{HL}} \simeq 0.2$ meV which is less than 10% of the overall δV_{HL} . This finding indicates the incorrect link between HH–LH mixing, in strain-free GaAs/AlGaAs QDs, and QD shape anisotropy [25].

Mechanism (iii) Intrinsic Nonequivalence of the $[110]$ and $[1\bar{1}0]$ Directions. The impact of QD shape anisotropy and alloy randomness on HH–LH coupling is fairly small, as discussed above. HH–LH coupling $\delta V_{\text{HL}} = 2.15$ meV of nominal C_{2v} GaAs QDs is thus mainly arising from the remaining mechanisms (iii) and (iv), i.e., intrinsic nonequivalence of the $[110]$ and $[1\bar{1}0]$ directions and low symmetry interfaces. Interface-induced HH–LH coupling is found to be $\delta V_{(\text{iv}),\text{HL}} = 0.8$ meV and intrinsic nonequivalent of the $[110]$ and $[1\bar{1}0]$ directions leads consequently to $\delta V_{(\text{iv}),\text{HL}} \simeq 1.35$ meV. Therefore, mechanisms (iii) and (iv) contribute 50–60% and 50–40%, respectively, of the HH–LH mixing in nominal C_{2v} GaAs QDs, depending on QD shape.

In conclusion, we comprehensively and quantitatively analyzes the impact of a total of six mechanisms leading to HH–LH mixing in semiconductor QDs. The novel quantum transmissibility of HH–LH mixing mediated by intermediate states is highlighted. We find that the HH–LH mixing in strain-free nominal D_{2d} GaAs QDs majorly arises from the mechanism (iv) low local symmetry interfaces with a HH–LH coupling $\delta V_{\text{HL}} = 0.8$ meV. In strain-free nominal C_{2v} GaAs QDs, mechanisms (iii) and (iv) related to atomistic interfaces and intrinsic nonequivalence

of the [110] and $[1\bar{1}0]$ directions contribute 50–60% and 50–40%, respectively, to the HH–LH mixing. The mechanism (ii) related to the QD shape anisotropy contributes less than 10%. In strained In(Ga)As/GaAs QDs, mechanism (i) given by built-in shear strain contributes 80% to the HH–LH mixing and the remaining 20% stems from intrinsic nonequivalence of the [110] and $[1\bar{1}0]$ directions and the interface effect in a ratio of 3:2. Most importantly thing the HH–LH mixing in strained QDs is mainly due to the quantum transmissibility of HH–LH mixing mediated by intermediate QD states. Since the HH–LH coupling δV_{HL} is nearly insensitive to the QD morphology for a type of QDs, the HH–LH mixing can only be tuned by designing QDs with specific HH–LH splitting Δ_{HL} . For nominal C_{2v} In(Ga)As/GaAs QDs (as shown in Fig. 14.11b), flatter QDs usually have larger HH–LH splitting and consequently smaller HH–LH mixing. This is a consequence of quantum confinement and built-in strain that tends to be larger in flat structures. Whereas, for nominal C_{2v} GaAs/Al(Ga)As QDs, the QD height is inefficient to tune the HH–LH mixing. The lens-shape GaAs QDs often exhibit larger HH–LH splittings than Gaussian-shape GaAs QDs and thus have weaker HH–LH mixing. Increasing the Ga composition of the barrier for GaAs/Al(Ga)As QDs leads to enhanced HH–LH splitting and to reduced HH–LH mixing.

References

- Poem, E., Shemesh, J., Marderfeld, I., Galushko, D., Akopian, N., Gershoni, D., Gerardot, B.D., Badolato, A., Petroff, P.M.: *Phys. Rev. B* **76**, 235304 (2007)
- Abbarchi, M., Kuroda, T.T., Mano, T., Sakoda, K., Mastrandrea, C., Vinattieri, A., Gurioli, M., Tsuchiya, T.: *Phys. Rev. B* **3**, 774 (2007)
- Hatami, F., Masselink, W.T., Schrottke, L., Tomm, J.W., Talalaev, V., Kristukat, C., Goñi, A.R.: *Phys. Rev. B* **67**, 085306 (2003)
- Koguchi, N., Ishige, K.: *Jpn. J. Appl. Phys.* **32**, 2052 (1993)
- Moison, J.M., Houzay, F., Barthe, F., Leprince, L., André, E., Vatel, O.: *Appl. Phys. Lett.* **64**, 196 (1994). <http://link.aip.org/link/?APL/64/196/1>
- Wang, Z.M., Liang, B.L., Sablon, K.A., Salamo, G.J.: *Appl. Phys. Lett.* **90**, 113120 (3 pp.) (2007). <http://link.aip.org/link/?APL/90/113120/1>
- Lee, J.H., Wang, Z.M., Strom, N.W., Mazur, Y.I., Salamo, G.J.: *Appl. Phys. Lett.* **89**, 202101 (3 pp.) (2006). <http://link.aip.org/link/?APL/89/202101/1>
- Wang, L., Krápek, V., Ding, F., Horton, F., Schliwa, A., Bimberg, D., Rastelli, A., Schmidt, O.G.: *Phys. Rev. B* **80**, 085309 (2009). <http://link.aps.org/doi/10.1103/PhysRevB.80.085309>
- Sonnenberg, D., Graf, A., Paulava, V., Hansen, W., Heyn, C.: *Appl. Phys. Lett.* **101**, 143106 (4 pp.) (2012). <http://link.aip.org/link/?APL/101/143106/1>
- Atkinson, P., Zallo, E., Schmidt, O.G.: *J. Appl. Phys.* **112**, 054303 (5 pp.) (2012). <http://link.aip.org/link/?JAP/112/054303/1>
- Rastelli, A., Stuffer, S., Schliwa, A., Songmuang, R., Manzano, C., Costantini, G., Kern, K., Zrenner, A., Bimberg, D., Schmidt, O.G.: *Phys. Rev. Lett.* **92**, 166104 (2004). <http://link.aps.org/doi/10.1103/PhysRevLett.92.166104>
- Wei, S.-H., Zunger, A.: *Phys. Rev. B* **49**, 14337 (1994)
- Bir, G., Pikus, G.: *Symmetry and Strain-Induced Effects in Semiconductors*. Wiley, New York (1974)
- Li, S.-S., Xia, J.-B.: *Phys. Rev. B* **55**, 15434 (1997)

15. Luo, J.-W., Franceschetti, A., Zunger, A.: *Phys. Rev. B* **78**, 035306 (2008)
16. Zhang, L., d'Avezac, M., Luo, J.-W., Zunger, A.: *Nano Lett.* **12**, 984 (2012)
17. d'Avezac, M., Luo, J.-W., Chanier, T., Zunger, A.: *Phys. Rev. Lett.* **108**, 027401 (2012)
18. Luo, J.-W., Chantis, A.N., van Schilfgaarde, M., Bester, G., Zunger, A.: *Phys. Rev. Lett.* **104**, 066405 (2010)
19. Bennett, A.J., Pooley, M.A., Stevenson, R.M., Ward, M.B., Patel, R.B., de la Giroday, A.B., Skold, N., Farrer, I., Nicoll, C.A., Ritchie, D.A., et al.: *Nat. Phys.* **6**, 947 (2010)
20. Ghali, M., Ohtani, K., Ohno, Y., Ohno, H.: *Nat. Commun.* **3**, 661 (2012)
21. Luo, J.-W., Singh, R., Zunger, A., Bester, G.: *Phys. Rev. B* **86**, 161302 (2012)
22. Fischer, J., Loss, D.: *Phys. Rev. Lett.* **105**, 266603 (2010)
23. Koudinov, A.V., Akimov, I.A., Kusrayev, Y.G., Henneberger, F.: *Phys. Rev. B* **70**, 241305 (2004)
24. Kowalik, K., Krebs, O., Lemaître, A., Gaj, J.A., Voisin, P.: *Phys. Rev. B* **77**, 161305 (2008)
25. Belhadj, T., Amand, T., Kunold, A., Simon, C.-M., Kuroda, T., Abbarchi, M., Mano, T., Sakoda, K., Kunz, S., Marie, X., et al.: *Appl. Phys. Lett.* **97**, 051111 (3 pp.) (2010)
26. Liao, Y.-H., Liao, C.-C., Ku, C.-H., Chang, Y.-C., Cheng, S.-J., Jo, M., Kuroda, T., Mano, T., Abbarchi, M., Sakoda, K.: *Phys. Rev. B* **86**, 115323 (2012)
27. Tonin, C., Hostein, R., Voliotis, V., Grousson, R., Lemaître, A., Martinez, A.: *Phys. Rev. B* **85**, 155303 (2012)
28. Wang, L.-W., Zunger, A.: *Phys. Rev. B* **51**, 17398 (1995)
29. Luo, J.-W., Li, S.-S., Xia, J.-B., Wang, L.-W.: *Appl. Phys. Lett.* **88**, 143108 (2006)
30. Luo, J.-W., Franceschetti, A., Zunger, A.: *Nano Lett.* **8**, 3174 (2008)
31. Luo, J.W., Franceschetti, A., Zunger, A.: *Phys. Rev. B* **79**, 201301 (2009)
32. Luo, J.-W., Franceschetti, A., Zunger, A.: *Nano Lett.* **9**, 2648 (2009)
33. Zhang, L., Luo, J.-W., Zunger, A., Akopian, N., Zwiller, V., Harmand, J.-C.: *Nano Lett.* **10**, 4055 (2010)
34. Luo, J.-W., Stradins, P., Zunger, A.: *Energy Environ. Sci.* **4**, 2546 (2011)
35. Bester, G., Nair, S., Zunger, A.: *Phys. Rev. B* **67**, 161306 (2003)
36. Bester, G., Zunger, A.: *Phys. Rev. B* **71**, 045318 (2005)
37. Luo, J.-W., Li, S.-S., Xia, J.-B., Wang, L.-W.: *Phys. Rev. B* **71**, 245315 (2005)
38. Luo, J.-W., Bester, G., Zunger, A.: *New J. Phys.* **11**, 123024 (2009)
39. Mlinar, V., Bozkurt, M., Ulloa, J.M., Ediger, M., Bester, G., Badolato, A., Koenraad, P.M., Warburton, R.J., Zunger, A.: *Phys. Rev. B* **80**, 165425 (2009)
40. Luo, J.-W., Zunger, A.: *Phys. Rev. Lett.* **105**, 176805 (2010)
41. Luo, J.-W., Zunger, A.: *Phys. Rev. B* **84**, 235317 (2011)
42. Bester, G.: *J. Phys. Condens. Matter* **21**, 023202 (2009)
43. Wang, L.-W., Zunger, A.: *Phys. Rev. B* **59**, 15806 (1999)
44. Franceschetti, A., Fu, H., Wang, L.-W., Zunger, A.: *Phys. Rev. B* **60**, 1819 (1999)
45. Pryor, C., Kim, J., Wang, L.W., Williamson, A.J., Zunger, A.: *J. Appl. Phys.* **83**, 2548 (1998)
46. Williamson, A.J., Wang, L.-W., Zunger, A.: *Phys. Rev. B* **62**, 12963 (2000)
47. Luo, J.-W., Bester, G., Zunger, A.: *Phys. Rev. B* **79**, 125329 (2009)
48. Keating, P.N.: *Phys. Rev.* **145**, 637 (1966)
49. Bester, G., Zunger, A.: *Phys. Rev. B* **72**, 165334 (2005)
50. Yurgaftman, I., Meyer, J.R., Ram-Mohan, L.R.: *J. Appl. Phys.* **89**, 5815 (2001)
51. Yu, P.Y., Cardona, M.: *Fundamentals of Semiconductors: Physics and Materials Properties*, 3rd edn. Springer, Berlin (2004)
52. Barrow, G.M.: *Introduction to Molecular Spectroscopy*, 3rd edn. McGraw-Hill, New York (1962)
53. Krenner, H.J., Clark, E.C., Nakaoka, T., Bichler, M., Scheurer, C., Abstreiter, G., Finley, J.J.: *Phys. Rev. Lett.* **97**, 076403 (2006)
54. Ester, P., Stuffer, S., de Vasconcellos, S.M., Bichler, M., Zrenner, A.: *Phys. Status Solidi (c)* **3**, 3722 (2006)
55. Sychugov, I., Juhasz, R., Valenta, J., Linnros, J.: *Phys. Rev. Lett.* **94**, 087405 (2005)

56. Abbarchi, M., Kuroda, T., Mano, T., Sakoda, K., Mastrandrea, C.A., Vinattieri, A., Gurioli, M., Tsuchiya, T.: *Phys. Rev. B* **82**, 201301 (2010)
57. Keizer, J.G., Bocquel, J., Koenraad, P.M., Mano, T., Noda, T., Sakoda, K.: *Appl. Phys. Lett.* **96**, 062101 (3 pp.) (2010)
58. Blokland, J.H., Bozkurt, M., Ulloa, J.M., Reuter, D., Wieck, A.D., Koenraad, P.M., Christensen, P.C.M., Maan, J.C.: *Appl. Phys. Lett.* **94**, 023107 (3 pp.) (2009)
59. Kumah, D.P., Wu, J.H., Hussein, N.S., Dasika, V.D., Goldman, R.S., Yacoby, Y., Clarke, R.: *Appl. Phys. Lett.* **98**, 021903 (3 pp.) (2011)
60. Abbarchi, M., Mastrandrea, C.A., Kuroda, T., Mano, T., Sakoda, K., Koguchi, N., Sanguinetti, S., Vinattieri, A., Gurioli, M.: *Phys. Rev. B* **78**, 125321 (2008)
61. Kuroda, K., Kuroda, T., Sakoda, K., Watanabe, K., Koguchi, N., Kido, G.: *Appl. Phys. Lett.* **88**, 124101 (3 pp.) (2006)
62. Jo, M., Mano, T., Sakoda, K.: *J. Appl. Phys.* **108**, 083505 (3 pp.) (2010)
63. Mano, T., Abbarchi, M., Kuroda, T., Mastrandrea, C., Vinattieri, A., Sanguinetti, S., Sakoda, K., Gurioli, M.: *Nanotechnology* **20**, 395601 (2009)
64. Abbarchi, M., Kuroda, T., Mastrandrea, C., Vinattieri, A., Sanguinetti, S., Mano, T., Sakoda, K., Gurioli, M.: *Physica E Low Dimens. Syst. Nanostruct.* **42**, 881 (2010)
65. Keizer, J.G., Jo, T.M.M., Noda, T., Sakoda, K., Koenraad, P.M.: *Appl. Phys. Lett.* **98**, 193112 (2011)
66. Mlinar, V., Zunger, A.: *Phys. Rev. B* **80**, 205311 (2009)
67. Ivchenko, E.L.: *Phys. Status Solidi (a)* **164**, 487 (1997)
68. Singh, R., Bester, G.: *Phys. Rev. Lett.* **104**, 196803 (2010)
69. Plumhof, J.D., Křápek, V., Wang, L., Schliwa, A., Bimberg, D., Rastelli, A., Schmidt, O.G.: *Phys. Rev. B* **81**, 121309 (2010)
70. Bayer, M., Ortner, G., Stern, O., Kuther, A., Gorbunov, A.A., Forchel, A., Hawrylak, P., Fafard, S., Hinzer, K., Reinecke, T.L., et al.: *Phys. Rev. B* **65**, 195315 (2002)
71. Benson, O., Santori, C., Pelton, M., Yamamoto, Y.: *Phys. Rev. Lett.* **84**, 2513 (2000)
72. Michler, P. (ed.): *Single Semiconductor Quantum Dots Series: NanoScience and Technology*. Springer, Berlin (2009)
73. Bayer, M., Kuther, A., Forchel, A., Gorbunov, A., Timofeev, V.B., Schäfer, F., Reithmaier, J.P., Reinecke, T.L., Walck, S.N.: *Phys. Rev. Lett.* **82**, 1748 (1999)
74. Warburton, R.J., Schaflein, C., Haft, D., Bickel, F., Lorke, A., Karrai, K., Garcia, J.M., Schoenfeld, W., Petroff, P.M.: *Nature* **405**, 926 (2000)
75. Takagahara, T.: *Phys. Rev. B* **62**, 16840 (2000)
76. Besombes, L., Kheng, K., Martrou, D.: *Phys. Rev. Lett.* **85**, 425 (2000)
77. Seguin, R., Schliwa, A., Rodt, S., Potschke, K., Pohl, U.W., Bimberg, D.: *Phys. Rev. Lett.* **95**, 257402 (2005)
78. Seidl, S., Kroner, M., Högele, A., Karrai, K., Warburton, R., Badolato, A., Petroff, P.: *Appl. Phys. Lett.* **88** (2006)
79. Plumhof, J.D., Křápek, V., Ding, F., Jöns, K.D., Hafenbrak, R., Klenovský, P., Herklotz, A., Dörr, K., Michler, P., Rastelli, A., et al.: *Phys. Rev. B* **83**, 121302 (2011)
80. Kowalik, K., Krebs, O., Lemaitre, A., Laurent, S., Senellart, P., Voisin, P., Gaj, J.A.: *Appl. Phys. Lett.* **86**, 041907 (2005)
81. Marcet, S., Ohtani, K., Ohno, H.: *Appl. Phys. Lett.* **96**, 101117 (2010)
82. Stevenson, R.M., Young, R.J., See, P., Gevaux, D.G., Cooper, K., Atkinson, P., Farrer, I., Ritchie, D.A., Shields, A.J.: *Phys. Rev. B* **73**, 033306 (2006)
83. Jundt, G., Robledo, L., Högele, A., Fält, S., Imamoğlu, A.: *Phys. Rev. Lett.* **100**, 177401 (2008)
84. Muller, A., Fang, W., Lawall, J., Solomon, G.S.: *Phys. Rev. Lett.* **103**, 217402 (2009)
85. Gong, M., Zhang, W., Guo, G.-C., He, L.: *Phys. Rev. Lett.* **106**, 227401 (2011)
86. Watanabe, K., Koguchi, N., Gotoh, Y.: *Jpn. J. Appl. Phys.* **39**, L79 (2000)
87. Young, R.J., Stevenson, R.M., Shields, A.J., Atkinson, P., Cooper, K., Ritchie, D.A., Groom, K.M., Tartakovskii, A.I., Skolnick, M.S.: *Phys. Rev. B* **72**, 113305 (2005)

88. Stevenson, R.M., Salter, C.L., Nilsson, J., Bennett, A.J., Ward, M.B., Farrer, I., Ritchie, D.A., Shields, A.J.: *Phys. Rev. Lett.* **108**, 040503 (2012)
89. Vogel, M.M., Ulrich, S.M., Hafenbrak, R., Michler, P., Wang, L., Rastelli, A., Schmidt, O.G.: *Appl. Phys. Lett.* **91**, 051904 (3 pp.) (2007)
90. Jaros, M.: *Rep. Prog. Phys.* **48**, 1091 (1985)
91. Trotta, R., Zallo, E., Ortix, C., Atkinson, P., Plumhof, J.D., van den Brink, J., Rastelli, A., Schmidt, O.G.: *Phys. Rev. Lett.* **109**, 147401 (2012)
92. Ladd, T.D.: *Physics* **5**, 109 (2012)
93. Li, S.-S., Xia, J.-B., Yuan, Z.L., Xu, Z.Y., Ge, W., Wang, X.R., Wang, Y., Wang, J., Chang, L.L.: *Phys. Rev. B* **54**, 11575 (1996)
94. Koster, G., Dimmock, J., Wheeler, R., Statz, H.: *Properties of the Thirty-Two Point Groups*. MIT, Cambridge (1963)
95. Magri, R., Zunger, A.: *Phys. Rev. B* **62**, 10364 (2000)
96. van Kesteren, H.W., Cosman, E.C., van der Poel, W.A.J.A., Foxon, C.T.: *Phys. Rev. B* **41**, 5283 (1990)
97. Chang, Y.-C., Schulman, J.N.: *Appl. Phys. Lett.* **43**, 536 (1983)
98. Ivchenko, E.L., Kaminski, A.Y., Rössler, U.: *Phys. Rev. B* **54**, 5852 (1996)
99. Winkler, R.: *Spin-Orbit Coupling Effects in Two-Dimensional Electron and Hole Systems*. Springer Tracts in Modern Physics, vol. 191. Springer, Berlin (2003)
100. Luttinger, J.M., Kohn, W.: *Phys. Rev.* **97**, 869 (1955)
101. Kane, E.O.: *J. Phys. Chem. Solids* **1**, 249 (1957)
102. Tanaka, T., Singh, J., Arakawa, Y., Bhattacharya, P.: *Appl. Phys. Lett.* **62**, 756 (1993)